ULTRA-THIN FLEXIBLE THERMAL GROUND PLANE MODELING AND EXPERIMENTAL EXAMINATION

A Thesis
Presented to
The Academic Faculty

by

Barbara Giffin

In Partial Fulfillment
of the Requirements for the Degree
Master of Science in the
George W. Woodruff School of Mechanical Engineering

Georgia Institute of Technology
December 2021

ULTRA-THIN FLEXIBLE THERMAL GROUND PLANE MODELING AND EXPERIMENTAL EXAMINATION

Approved by:

Dr. G.P. Peterson, Advisor
School of Mechanical Engineering
Georgia Institute of Technology

Dr. Zhuomin Zhang
School of Mechanical Engineering
Georgia Institute of Technology

Dr. Peter Loutzenhiser
School of Mechanical Engineering
Georgia Institute of Technology

Dr. Yogendra Joshi
School of Mechanical Engineering
Georgia Institute of Technology

Date Approved: [Nov. 18, 2021]

ACKNOWLEDGEMENTS

I would like to especially thank my advisor, Dr. Peterson, for his trust and willingness to work with me from across the country. Without his support and open mind I may not have had the chance to complete a thesis as a distance learning student. I would also like to thank the SMART Scholarship program and Navy for investing in my future. Finally, I would like to thank my family and friends for their never-ending support.

TABLE OF CONTENTS

LIST OF TABLES

LIST OF FIGURES

LIST OF SYMBOLS AND ABBREVIATIONS

A	Area
CPU	Central Processing Unit
d	Discretization Dimension
FLIR	Forward Looking Infrared
g	Gravity
h	Height
ΔH_{vap}	Latent Heat of Vaporization
k	Permeability
L	Length
LP	Liquid Pillar
Ma	Mach
N	Number of Measurements
P	Perimeter
ΔP	Pressure Drop
q	Flux
r	Radius
R	Resistance
Re	Reynold's
s	Standard Deviation
SU	Standard Uncertainty
T	Temperature
TGP	Thermal Ground Plane

v	Velocity
VP	Vapor Pillar
w	Groove Width
We	Weber Number

Greek Symbols

δ	Groove Depth
δx	Uncertainty of Each Measurement
ϵ	Porosity
λ	Thermal Conductivity
μ	Viscosity
ρ	Density
σ	Surface Tension
ψ	Hydrostatic Angle

SUMMARY

Electronic industry increasing thermal loads necessitate updated, more adequate thermal management techniques. Thermal Ground Planes (TGPs) use phase change to achieve high conductivities and effectively spread heat over their flat geometries. Multiple configurations are possible for these TGPs, as their internal structures may be as simple or complex as necessary to achieve the desired heat transport capacity. Kelvin Thermal is a startup business located in Boulder, Colorado that manufactures multiple TGP geometries for various applications, especially for the electronics industry. They currently use basic, hand-calculation tools to design and examine new configurations. They also manufacture and test TGPs to better understand their full capabilities. The objective of this effort is to develop a TGP design tool for Kelvin Thermal. This design tool calculates important parameters in a timely fashion, providing a re-usable tool for design and taking the place of hand calculations. Multiple input variables and configuration parameters provide flexibility, allowing engineers to compare the functionality of different designs for each application. Comparing design tool results to measured test results, also obtained in this effort, provides insight into model accuracy and useful adjustment factors. Adjustment factors provide additional design tool functionality, accounting for heat losses and assumptions. With these adjustment factors, the design tool calculates both theoretical best-case results as well as sensible estimates, both of which provide useful information to a design engineer. Final versions of the model correlate well with measured conductivities with a difference of 3.7%, and measured temperatures when adjusted for emissivity with a difference of less than 1%.

CHAPTER 1. INTRODUCTION

Thermal ground planes (TGPs) provide excellent heat spreading capabilities across their flat, 2D geometries. With effective conductivities on the order of 10 to even 60 times that of copper, these phase change heat spreaders have multiple applications, especially in the electronics industry. As electronics become more robust, higher heat loads in smaller components require modernized cooling and heat spreading techniques. Different applications require various designs to achieve the optimal heat spreading capabilities. Kelvin Thermal designs TGPs to meet these numerous requirements, while manufacturing new designs to gain experimental knowledge. TGP designs vary through an assortment of geometric and internal parameters including overall geometry and size, wick type, wick configuration (single or stacked wick), liquid pillar type, working fluid, etc. With countless configuration possibilities, manufacturing and testing each configuration becomes expensive and unrealistic. A verified analytical model providing the ability to vary all important design parameters, and calculating vital TGP characteristics such as thermal conductivity and maximum transport capacity, provides a design tool saving the engineer time and money.

1.1 Literary Review of Existing Models

Liu et al. develop a "reduced order thermo-fluidic model to predict the effect of both heat flux and liquid charge" [1] of a vapor chamber. Fluid sub-models provide information for each section independently (evaporator, condenser, and vapor core), then a solid conduction model calculates overall resistance and thermal performance of the system. Adapting a similar approach for this case, with necessary changes to provide an

accurate model of the TGP structure and heat flow, provides a realistic TGP design tool. Figure 1 provides a comparison of vapor chamber and TGP structures and heat flows.

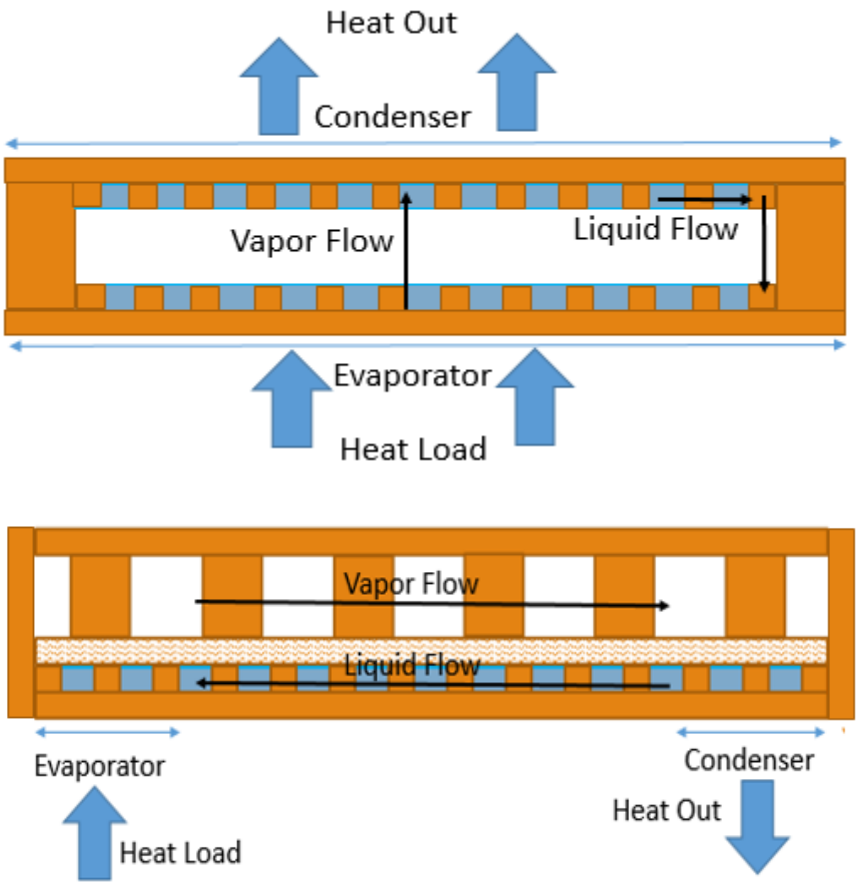

Figure 1 – Operation overview. Top: Vapor chamber, Bottom: TGP

Liu et al. [1] divides the thermal conductivity of the system into two sections. One section includes the side walls of the system, and the other includes the active part of the system where flow occurs. An estimated heat flux value provides the start to an iterative process. Individual conductivities of the evaporator, condenser, and vapor core sections are calculated based on the estimated flux value. Known material conductivities and geometries provide an estimate for the outer wall thermal conductivity. Then, by comparing the overall heat flux value and estimated value an iterative process ensues until

these flux values converge. Total resistance calculations provide a 3D temperature distribution. The TGP design tool produced in this effort includes similar iterative calculations with necessary adjustments for the geometries which don't occur in a vapor chamber. The vapor chamber flow direction differs from the TGP flow direction as well, with vapor chamber conducting heat through its thickness and TGPs spreading heat axially (Figure 1). The design tool accounts for this with axial thermal conductivity calculations.

Lewis et al. [2] also model overall thermal performance of a TGP. They state that axial resistance values through both the mesh and the siding material are orders of magnitude larger than the total resistance of the system, and thus "only a 1-dimensional path of heat flow must be analyzed" [2]. A resistance network then calculates an effective thermal conductivity of the system, which quantifies TGP effectiveness (Figure 2). Lewis et al. [2] analyze a horizontal one-dimensional path for heat flow, while Liu et al. [1] examine a more complex, two-dimensional, path. Their analysis includes a resistance network for each micro-pillar cell within the evaporator and condenser, provided in Figure 3, in combination with an axial network similar to the Liu et al. approach. They consider five resistance values through each micro-pillar cell including thin-film resistances of the thin region of fluid in contact with the top of the liquid pillars, interfacial resistances between fluid and vapor, and bulk resistances of the liquid and liquid pillars. In addition to these device-level macro models, Ranjan et al. [3] develop a detailed wick micro-level model to account for liquid-vapor interface resistance. A mix of these approaches provides useful thermal performance estimations for this application, detailed in Sections 2.4.1 and 2.4.2.

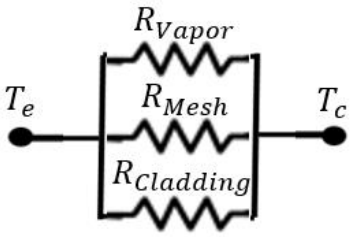

Figure 2 – Lewis et al. resistance network overview.

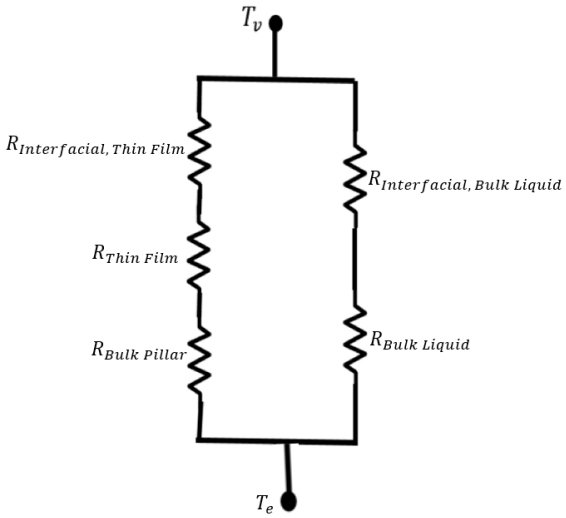

Figure 3 – Liu et al. resistance network overview.

The 3D transient model designed by Patankar et al. [4] makes use of both analytical analysis, for the space dimension, as well as numerical analysis for the time dimension. Unlike previously mentioned studies, the numerical analysis for the time dimension allows the model to use temperature dependent properties for the fluid and vapor, as well as calculate a transient response. This method calculates three dimensional transient fields of temperature, pressure, and fluid/vapor velocities. They conclude that "traditional practices for optimization of the vapor chamber wall, wick, and vapor-core thicknesses under steady-state conditions, cannot be directly used under transient conditions" [4]. As this effort provides a general design tool, steady-state conditions suffice to provide details on TGPs

with fairly steady and consistent heat loads. As Patankar et al. point out though, the engineer must be cautioned about the accuracy of steady-state results for transient heat load applications where initial responses become important.

Hybrid geometry of the TGP provides an important distinction between the previously mentioned sources and this effort. The TGP contains vapor pillars, unlike the vapor cores previously discussed, as well as a hybrid wicking structure, not addressed by Lewis et al. [2]. Ravi et al. [5] examine the effects of various hybrid wicking structures on capillary transport. Hybrid wicking structures contain both liquid wick pillars and a wicking structure, changing the wick/liquid interaction. “The drawbacks of homogeneous wicks can be overcome by utilizing hybrid wicks with two or more pore sizes, such that the smaller pores generate a high capillary pressure and the larger pores increase wick permeability” [5]. TGP hybrid wicking structures make use of a liquid wick mesh with small pore sizes on top of liquid wick pillars with larger pore sizes. Ravi et al. [5] refer to this configuration as an “out-of-plane hybrid wick”. They explain that this mesh configuration has a low dry-out threshold, since the fluid levels must be larger than the liquid pillar height to wet the wick, but a thicker mesh increases this limit. Thicker meshes also increase thermal resistance in the system, so mesh thickness must be optimized for each configuration. Although the dry-out threshold limits TGP capabilities, these hybrid wicking structures provide high capillary pressure and permeability while minimizing thermal resistance of the fluid/wick system [5]. This effort examines hybrid wicking structure impacts on the TGP performance.

Overall, current literature examines various numerical models. These numerical models provide important insight into vapor chamber and TGP performance, but each focus

on the importance of modeling specific characteristics such as micro-level modeling or vapor flow. This effort makes use of literature to determine the most important design tool parameters to include, while providing an overall design tool applicable to countless configurations, unlike previous works.

1.2 Thermal Ground Plane (TGP) Overview

Kelvin Thermal, located in Boulder, Colorado, manufactures the TGPs used in this effort. These TGPs are thin and flexible, with a thickness of 0.3 mm and a minimum bending radius of 3-10 mm (Figure 4). They have high conductivities ranging from 4,000 to 25,000 W/m·K [6], depending on the configuration. Kelvin Thermal manufactures various sizes for application to small or large electronics. For this effort, Kelvin Thermal supplied four samples each with similar characteristics. These 44 mm by 106 mm copper-water TGPs contain side cladding, liquid pillars, a liquid mesh, and vapor pillars (Figure 5).

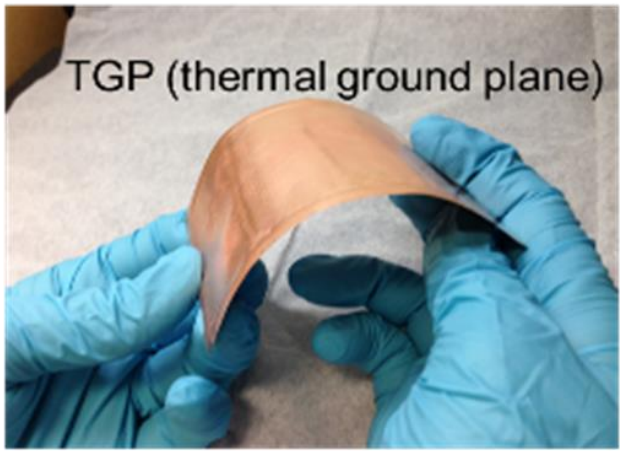

Figure 4 – TGP bending visual with minimum bending radius of 3-10 mm.

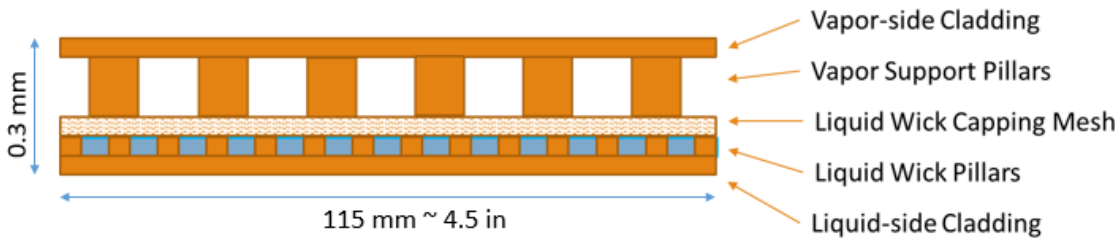

Figure 5 – TGP sectional overview.

TGPs provide effective heat spreading by use of liquid phase change and capillary pressure. A heat load applied to any section of the TGP forms an evaporator section. In this section, fluid evaporates and the remaining fluid recedes into the wick causing a small contact angle. Due to a pressure gradient across the system, vapor flows away from the evaporator section toward the condenser section, which extracts heat from the system. In this section, fluid condenses once again and fills the wick. The difference in fluid contact angles across the system causes a capillary pressure distribution which forces fluid flow from the full condenser side back to the evaporator through the porous wick and liquid pillars.

CHAPTER 2. DESIGN TOOL THEORY

2.1 Variable Inputs

A number of design features are of particular interest to Kelvin Thermal. These features include mesh type (woven especially), two stacked mesh types (with the finer mesh on top), overall geometries, and variable liquid pillar geometries with the option for no liquid pillars. The input section of the design tool provides variability of all parameters listed above as well as evaporator and condenser sizes and locations.

Geometric inputs include large-scale details such as overall TGP dimensions and materials, as well as mesh and liquid/vapor pillar specifics. Through varying mesh dimensions in the form of pore size and wire thickness, the design tool accounts for many different mesh types. Specifying a mesh geometry in place of the liquid pillar geometries models two stacked mesh types. Overall geometries are variable as well as wall thicknesses on all sides. A rectangular TGP geometry assumption leads to an effective working/active region calculation, used for more detailed analyses within the TGP (Figure 6). For the case void of liquid pillars, the user may specify the liquid pillar heights as approaching zero and their spacing and shape values as discretization dimensions (discussed in Section 2.2). Vapor pillar geometries and cladding thickness are also variable. Figure 6 and Figure 7 detail TGP geometric features.

Figure 6 – TGP active region, top view.

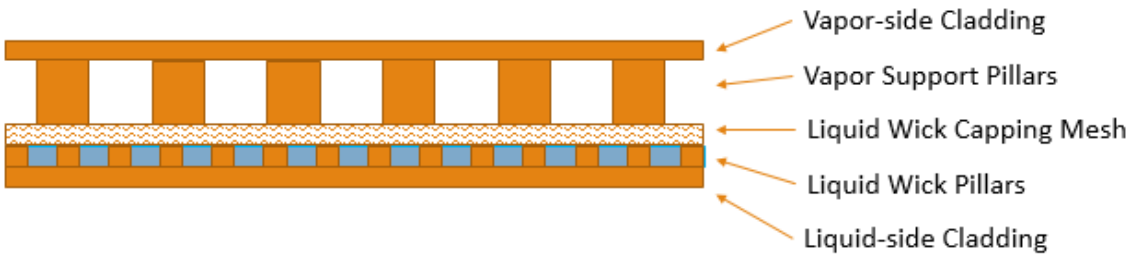

Figure 7 – TGP cross-sectional view.

2.2 Discretization

Discretization of the TGP permits calculation of varying parameters along the TGP length such as resistances, contact angles, pressures, etc. The design tool breaks the TGP into sections in the planar flow direction, denoted as the x-direction. Discretization occurs along the center lines of the liquid pillars, as they commonly have a larger natural length scale than the mesh which lends itself to discretization. If no liquid pillars are present, the user may specify the height of the liquid pillars to be essentially zero and specify the liquid pillar dimensions in the x-direction to correlate with desired cell size. Figure 8 and Figure 9 provide discretization visuals.

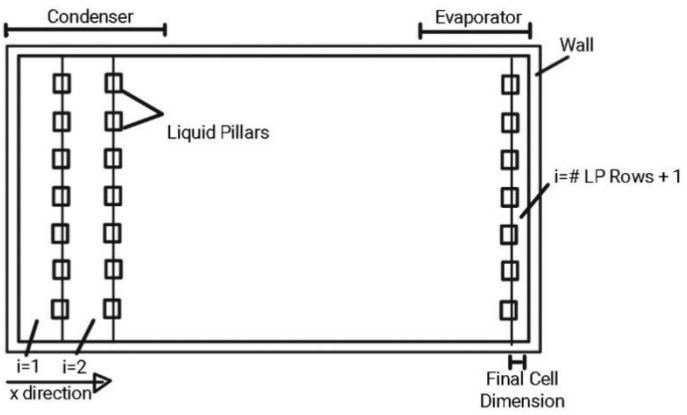

Figure 8 – TGP discretization top view.

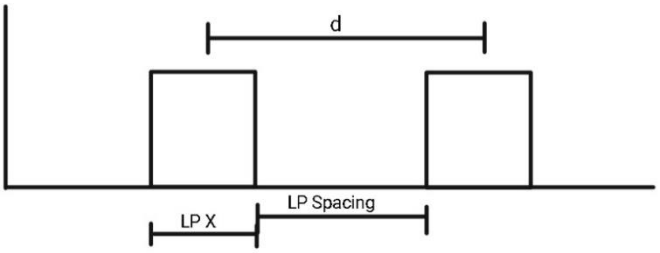

Figure 9 – TGP discretization side view.

The design tool establishes a dimension (d) as the discretization length where:

$$d = LP\ X + LP\ Spacing \tag{1}$$

With the liquid pillar thickness in the x direction denoted as ($LP\ X$) and spacing between liquid pillars ($LP\ Spacing$). Cells are then formed along the x-direction of the TGP within the active region, beginning on the condenser side of the TGP. The following equation provides an estimation for the total number of cells:

$$Estimated\ Cells = \frac{Total\ Active\ X}{d}, rounded\ down \tag{2}$$

If the discretization length does not perfectly divide the active length, the final cell dimension makes up the difference, as seen in Figure 8.

$$Last\ Cell\ d = \ Total\ Active\ X - Estimated\ Cells * d \tag{3}$$

The total number of cells then becomes:

$$Total\ \#\ Cells = Estimated\ Cells + 1 \tag{4}$$

A check point verifies that the discretization lengths of all cells sum to the total active length before moving on the other sections of the code.

$$Check\ That: Total\ Active\ X = (Total\ \#\ Cells - 1) * d + Last\ Cell\ d \tag{5}$$

If the above statement reads true, an output occurs stating that the discretization was successful.

2.3 Maximum Transport Capacity

2.3.1 Capillary Limitation

Peterson [7] describes capillary limitation with the following statement. “For a heat pipe to function properly, the net capillary pressure difference between the wet and dry points…must be greater than the summation of all the pressure losses occurring throughout the liquid and vapor flow paths” [7]. Kelvin Thermal expresses interest in understanding the capillary pressure limit of various TGPs. This limit provides important insight into TGP heat transport capacity.

A balance of capillary pressure at the liquid-vapor interface with the summation of essential pressure drops within the system is used to derive this limit. These pressure drops include vapor pressure drop, liquid pressure drop, pressure drop at the phase transition, and normal and axial hydrostatic pressure variations. Peterson states, "While these terms may be important in the modeling and analysis of very small heat pipes, the combined effect of the mass flux at the interface and interfacial surface curvature produces a phase transition pressure gradient that typically can be neglected" [7]. Therefore, this effort incorporates all pressure-drop terms except the pressure drop at the phase transition. The design tool attempts to provide a good estimation for capillary pressure limit on maximum transport capacity, so the phase transition pressure drop is neglected as it has minimal impact on the result. The general equation for this capillary pressure limit follows:

$$\begin{aligned} Capillary\ pressure\ at\ liquid/vapor\ interface \\ = Vapor\ pressure\ drop + Liquid\ pressure\ drop \\ + Normal\ hydrostatic\ pressure\ drop \\ + Axial\ hydrostatic\ pressure\ drop \end{aligned} \tag{6}$$

Denoted as:

$$\Delta P_{c,m} = \Delta P_v + \Delta P_l + \Delta P_{h_{normal}} + \Delta P_{h_{axial}} \tag{7}$$

Sections 2.3.1.1 through 2.3.1.5 detail each term individually.

2.3.1.1 Capillary Pressure at Liquid/Vapor Interface

The difference between vapor pressure and liquid pressure results in a capillary pressure at the liquid/vapor interface. Surface tension and effective capillary radii in the condenser and evaporator drive the capillary pressure difference across the TGP. Peterson [7] gives the following equation, assuming the capillary radius in the condenser during steady-state operation approaches infinity, a common assumption.

$$\Delta P_{c,m} = \frac{2\sigma}{r_{c,e}} \tag{8}$$

With variables: maximum capillary pressure ($\Delta P_{c,m}$), surface tension (σ), and effective capillary radius of the evaporator wick ($r_{c,e}$).

A water properties table [8] provides surface tension, taken at an average liquid temperature within the evaporator section. General conductance calculations provide an estimate for average liquid temperature with the following equations:

$$T_{inside\ cladding} = \frac{q_{max} * cladding\ thickness}{\lambda_{cladding} * A_{evaporator}} + T_{room} \tag{9}$$

$$T_l = \frac{T_v + T_{inside\ cladding}}{2} \tag{10}$$

With maximum transport (q_{max}) and thermal conductivity of the cladding ($\lambda_{cladding}$). These equations depend on the ambient air temperature, an initial guess for vapor temperature, and an initial guess for maximum flux. The estimated/guessed terms for vapor

temperature and maximum flux update with future iterations, as explained in section 2.3.1.5.

Peterson [7] provides an equation for the effective capillary radius of wire screens as:

$$r_{c,e} = \frac{wire\ spacing + wire\ diameter}{2} \tag{11}$$

The above equation uses corresponding mesh geometries to calculate the effective capillary radius of the evaporator wick. Then, Equation 8 calculates the capillary pressure at the liquid/vapor interface.

2.3.1.2 Vapor Pressure Drop

The vapor pressure drop term provides information about in-plane vapor pressure distribution (x-direction). Peterson states, "This variation in vapor pressure is principally the result of the viscous pressure drop occurring along the vapor flow path" [7]. The following equation calculates the vapor pressure drop.

$$\Delta P_v = \left(\frac{C(f_v Re_v)\mu_v}{2\left(r_{h,v}\right)^2 A_v \rho_v \Delta H_{vap}} \right) L_{eff} q \tag{12}$$

The estimated vapor temperature and properties table provide viscosity (μ_v), density (ρ_v), and latent heat of vaporization (ΔH_{vap}) values. Cell length (d) sets effective length (L_{eff}) for each cell. Equation 13 calculates the vapor flow cross sectional area, approximating the area as channels between vapor pillars.

$$A_v = VP_z * active_y - VP_{diam} * VP_z * \#VP\ in\ y \tag{13}$$

With vapor pillars (VP), subscript z as height, and the number of vapor pillars in y calculated simply with the active length divisible by vapor pillar dimensions and distances. Cross sectional flow area divided by wetted perimeter describes the hydraulic radius of the vapor space.

$$r_{h,v} = \frac{A_v}{WettedP} \tag{14}$$

The wetted perimeter uses the same channel approximation as the cross-sectional flow area.

$$WettedP = VP_z * (2 + 2 * \#VP\ in\ y) + (total\ active\ y - (VP_{diam} * \#VP\ in\ y)) \tag{15}$$

The constants C and $f_v Re_v$ depend on the Reynolds and Mach numbers of the flow. Peterson [7] provides the following equations for Mach number and Reynolds number as well as estimates for these constants under various Mach and Reynolds number ranges.

$$Ma_v = \frac{q}{A_v \rho_v \Delta H_{vap} (R_v T_v \gamma_v)^{\frac{1}{2}}} \tag{16}$$

$$Re_v = \frac{2(r_{h,v})q}{A_v \mu_v \Delta H_{vap}} \tag{17}$$

$$Re_v < 2300, Ma_v < 0.2 : (f_v Re_v) = 16, C = 1 \tag{18}$$

$$Re_v < 2300, Ma_v > 0.2 : (f_v Re_v) = 16, C = \left[1 + \frac{\gamma_v - 1}{2} Ma_v^2\right]^{-\frac{1}{2}} \quad (19)$$

$$Re_v > 2300, Ma_v > 0.2 : (f_v Re_v) = 0.038 \left(\frac{2(r_{h,v})q}{A_v \mu_v \Delta H_{vap}}\right)^{\frac{3}{4}}, C = 1 \quad (20)$$

As seen above, the Reynolds number (Re_v) and Mach number (Ma_v) both depend on the estimated flux value. An initial guess for this value provides the information to calculate these numbers, and an iterative process ensues to calculate the maximum flux value limited by capillary pressure. All values taken from vapor tables are evaluated at the initial estimate for vapor temperature and updated through the iterative process. The above terms provide all necessary information to calculate an estimated vapor pressure drop across the TGP.

2.3.1.3 Liquid Pressure Drop

Like the vapor pressure drop term, viscous and inertial forces drive the liquid pressure drop resisting capillary flow through the wick and liquid pillars. For constant heat addition, Peterson [7] gives the following equation to calculate liquid pressure drop across the system.

$$\Delta P_l = \left(\frac{\mu_l}{k_T A_w \Delta H_{vap} \rho_l}\right) L_{eff} q \quad (21)$$

The estimated fluid temperature and properties tables provide viscosity (μ_l), density (ρ_l), and latent heat of vaporization (ΔH_{vap}) values. Cell length (d) provides the effective length

value (L_{eff}). The permeability (k_T) calculation for this hybrid wicking structure makes use of the individual component's permeability values weighted by their heights with the following equation [9].

$$k_T = \frac{k_1 A_1}{A_T} + \frac{k_2 A_2}{A_T} \tag{22}$$

Where the subscript T corresponds to a total value and subscripts 1 and 2 correspond to the mesh and liquid pillars respectively. Equation 23 gives the woven mesh permeability [7].

$$k_1 = \frac{d^2 \epsilon^3}{122(1-\epsilon)^2} \tag{23}$$

With the wire diameter as (d) and porosity (ϵ) given by:

$$\epsilon = \frac{Pore\ Volume}{Total\ Volume} \tag{24}$$

Equation 25 gives the liquid pillar permeability with a channel-like geometry assumption. This assumption allows the use of a general permeability calculation given in literature. A channel permeability equation calculates a reasonable estimation for this more complex liquid pillar geometry.

$$k_2 = \frac{2\epsilon r_{h,l}^2}{f_l Re_l} \tag{25}$$

Here, the constant $f_l Re_l$ depends on passage shape and is extrapolated from Peterson's Figure 3.5 for rectangular channels [7]. A rectangular groove geometry assumption also provides a good estimation for the hydraulic radius ($r_{h,l}$) with the following equation.

$$r_{h,l} = \frac{A_w}{P_w} \approx \frac{2w\delta}{w + 2\delta} \tag{26}$$

Here, the cell width (d) gives the groove width (w) and the liquid pillar height gives groove depth (δ). With these individual permeability values for the mesh and liquid pillars, equation 22 calculates an effective permeability value for the hybrid wicking structure. Then, equation 21 provides a liquid pressure drop value across the system with an iterative quality as stated previously.

2.3.1.4 Hydrostatic Pressure Drop

Hydrostatic pressure drop occurs within the TGP in the normal and axial directions due to gravitational effects. When at a non-horizontal angle, as in Figure 10, the pressure drop contributes to liquid pressure and decreases vapor pressure linearly with the evaporator located below the condenser. This pressure drop also contributes to dry-out, especially as the evaporator height above the condenser increases.

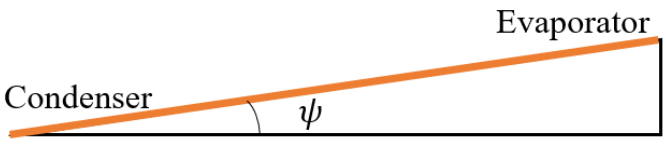

Figure 10 – Angle from horizontal with evaporator higher than condenser.

Hydrostatic pressure drop occurs in both the normal and axial directions, described by equations 27 and 28 respectively [7].

$$\Delta P_{h_{normal}} = \rho_l g d_v \cos(\psi) \tag{27}$$

$$\Delta P_{h_{axial}} = \rho_l g L \sin(\psi) \tag{28}$$

With the angle (ψ) set as worst-case 90 degrees, vapor diameter (d_v) set to vapor pillar height, and L set to the active length in the x-direction.

2.3.1.5 Maximum Heat Capacity

Substituting each pressure drop term into the overall pressure balance equation 30 gives the following.

$$\Delta P_{c,m} = \Delta P_v + \Delta P_l + \Delta P_{h_{normal}} + \Delta P_{h_{axial}} \tag{29}$$

$$\frac{2\sigma}{r_{c,e}} = \left(\frac{C(f_v Re_v)\mu_v}{2(r_{h,v})^2 A_v \rho_v \Delta H_{vap}}\right) L_{eff} q_{updated} + \left(\frac{\mu_l}{k_T A_w \Delta H_{vap} \rho_l}\right) L_{eff} q_{updated} + \rho_l g d_v \cos(\psi) + \rho_l g L \sin(\psi) \tag{30}$$

A guessed value of flux provides temperature-dependent values such as Mach, vapor and liquid properties, and constant values. The above equation then provides an updated flux value $(q_{updated})$ from the liquid and vapor pressure drop terms. Comparing the guessed and updated flux values, an iterative process ensues until the difference between these values becomes less than 0.1W. The final flux value describes the capillary limitation of the TGP.

2.3.2 Entrainment Limitation

Viscous forces between liquid flowing one direction and vapor flowing in the opposite direction may slow the return of liquid back to the evaporator. In extreme cases, liquid can become trapped in the vapor limiting the TGP's overall effectiveness. The entrainment limitation encompasses these scenarios, making use of the Weber number, or the ratio of viscous shear forces to surface tension forces [7]. Entrainment may occur when the Weber number becomes larger than one. The tool uses Equation 31 to calculate vapor velocity then calculates the Weber number with Equation 32 [7].

$$V_v = \frac{q}{A_v \rho_v \Delta H_{vap}} \tag{31}$$

$$We = \frac{2 r_{h,w} \rho_v V_v^2}{\sigma} \tag{32}$$

A printout notifies the user that "no entrainment occurs" if the Weber number remains less than one, otherwise a "check for entrainment" warning cautions the user to possible entrainment limitations.

2.4 Temperature Profiles

Detailed thermal resistance calculations for each cell provide an axial temperature response to a user-specified flux using the following general equation.

$$\Delta T = R * Q \tag{33}$$

Two-dimensional resistance values are calculated, both through the thickness of the TGP and axially. Resistance values of the vapor, wick, and pipe wall sections within each cell provide an axial temperature contour from the evaporator to the condenser of the TGP. More detailed through plane resistances in the evaporator and condenser sections provide additional information about evaporation and thin-film resistance effects. These resistance calculations are based on Peterson's equivalent resistances [7] with additional detail incorporated from Liu et al. [1] within the evaporator and condenser sections.

2.4.1 Through Plane Resistance

Liu et al. [1] describes a thermal resistance network applicable to liquid pillar geometries. Although their work characterizes vapor chamber thermal responses, the thermal resistance network provides important insight into liquid pillar resistance calculations. Their specified network breaks the through-plane resistance into detailed parts including: micropillar, bulk liquid, thin-film, and interfacial resistances for both the thin-film and bulk liquid regions. Peterson states that the interface resistance values are much smaller than other resistances comparatively, on the order of 10^{-5}, so the interfacial resistance values are excluded here. The remaining resistance values describe the liquid pillar section. Additional resistances through the outer wall and wick complete the thermal resistance network in the through plane direction. Person provides general equations for such resistances [7]. Figure 11 provides the through-plane resistance diagram used in both the evaporator and condenser sections of the design tool. Table 1 provides individual resistance details.

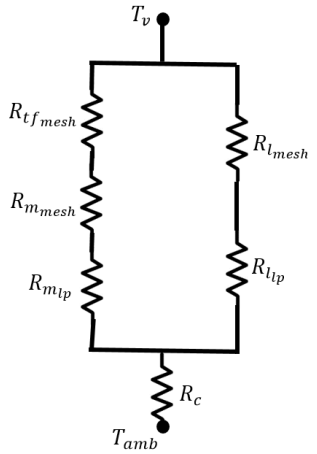

Figure 11 – Through plane resistance network.

Table 1 – Individual resistance details: Through plane.

R_c	Outer cladding through plane resistance: $$R_c = \frac{thickness}{\lambda A} \quad (34)$$ The current configuration incorporates two materials in the outer cladding and thus two different resistance calculations ensue for each material's thermal conductivity (λ) and thickness. Evaporator or condenser areas provide a value for A, correlating with the cell location.
R_l	Bulk liquid resistance: $$R_l = \frac{thickness}{\epsilon d^2 \lambda_{liquid}} \quad (35)$$ The liquid pillars and mesh have different bulk liquid resistance values, calculated using their corresponding thickness and porosity values.

Table 1 Continued

R_m	Bulk material pillar/mesh resistance: $$R_m = \frac{thickness}{(1-\epsilon)d^2\lambda_{material}} \quad (36)$$ The liquid pillars and mesh have different bulk material resistance values corresponding to their different porosity and material thermal conductivity values
R_{tf}	Thin-film resistance: $$R_{tf} = \frac{0.1h_{mesh}}{\lambda_l A_{tf}} \quad (37)$$ Thin film resistance only applies to the mesh, as the liquid pillars are saturated and have no thin film area. Ten percent of the mesh height (h_{mesh}) provides and estimation of thin film height. Ranjan et al. [3] provides an estimate for thin film area percentage relating to volume of square packed cells for different contact angles. Interpolation of this data provides an estimate for the thin film area.

2.4.2 Axial Resistance

In the axial direction, individual resistances for the vapor, wicking structure, and wall within each cell provide an overall axial temperature distribution. Above through plane resistance calculations, along with the user input flux value, provides initial evaporator temperature. Then, the axial resistance network provided in Figure 12 calculates the next cell temperature moving toward the condenser. Repetition of this process provides

temperature distribution across the entire TGP. These axial resistance values are calculated per unit length.

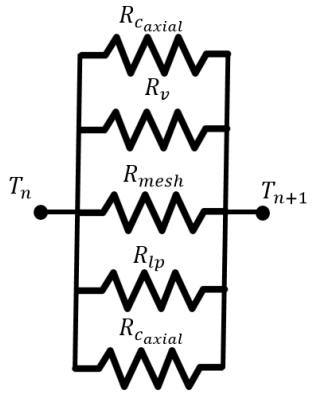

Figure 12 – Axial resistance network.

Table 2 – Individual resistance details: Axial.

$R_{c_{axial}}$	Outer cladding axial resistance: $$R_{c_{axial}} = \frac{1}{\lambda A} \quad (38)$$ The current configuration incorporates two materials into the outer cladding and thus two different resistance calculations ensue for each material's thermal conductivity and thickness.
R_{lp}	Liquid pillar axial resistance: $$R_{lp} = \frac{1}{\lambda_{eff_{lp}} A} \quad (39)$$ The liquid pillar section includes both liquid and liquid pillar material, requiring an effective thermal conductivity calculation.

Table 2 Continued

	Peterson [7] provides effective thermal conductivity equations for various wicking structures. For the liquid pillar configuration, the wick and liquid in series equation follows: $$\lambda_{eff_{lp}} = \frac{\lambda_l \lambda_w}{\epsilon \lambda_w + \lambda_l (1-\epsilon)} \quad (40)$$ This equation makes use of the detailed porosity calculation explained in the previous section.
R_{mesh}	Mesh axial resistance: $$R_{mesh} = \frac{1}{\lambda_{eff_{mesh}} A} \quad (41)$$ Similar to the liquid pillar axial resistance, the mesh requires an effective thermal conductivity calculation.
R_v	Vapor axial resistance: $$R_v = \frac{T_v(\Delta P_v)}{\rho_v \Delta H_{vap} q} \quad (42)$$ Through plane resistance calculates a vapor temperature estimate to use in this calculation. This resistance is extremely small, on the order of 10^{-8} compared to the other resistance values.

2.4.3 Two-Dimensional Application

Above theory examines a one-dimensional temperature distribution, assuming the condenser and evaporator span the entire width of the TGP and are located on opposite ends. This theory extends to a two-dimensional temperature distribution with a few user inputs and general assumptions. First, the user specifies evaporator center location, size, and heat load. Limiting the evaporator location to the bottom right quadrant accounts for symmetric geometries (Figure 13).

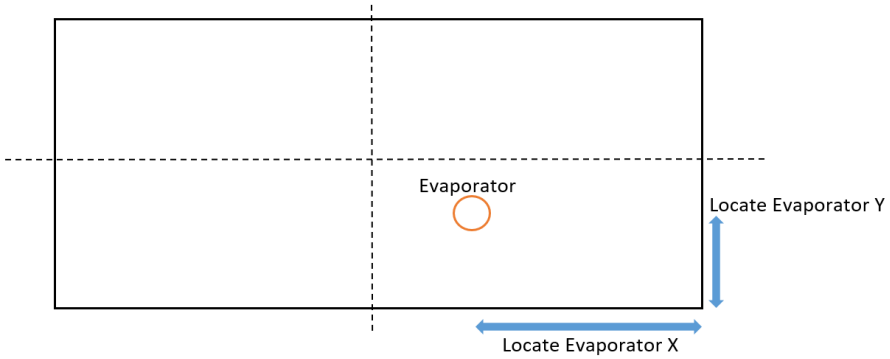

Figure 13 – Evaporator location, user specified values.

The model assumes a condenser location furthest away from the evaporator, allowing heat to spread across the entire TGP. The above, one-dimensional theory for calculating temperature across the TGP applies to the new setup, with a shorter "active length" ranging from the evaporator to the condenser (Figure 14).

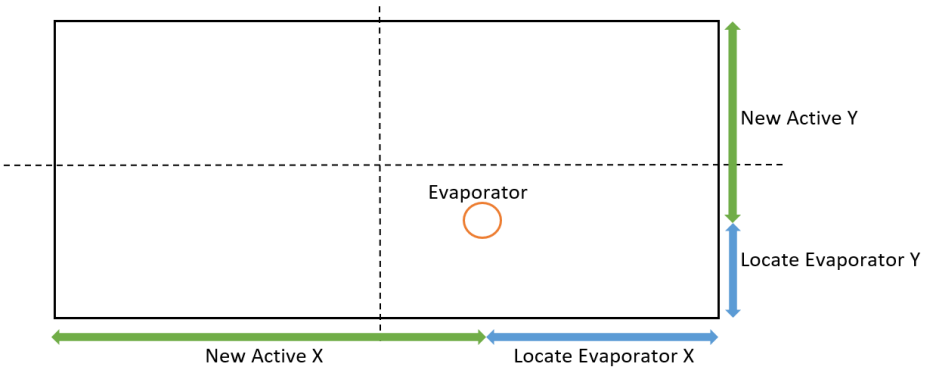

Figure 14 – Updated active lengths.

Finally, radially mapping the calculated one-dimensional temperature from the evaporator provides a full two-dimensional temperature profile.

2.4.4 Example Profiles

Figure 15 through Figure 18 provide both 1D and 2D temperature profiles of four different configurations. For smaller evaporators causing two-dimensional profiles, one-dimensional profiles are shown parallel to the x-axis intersecting the center of the evaporator.

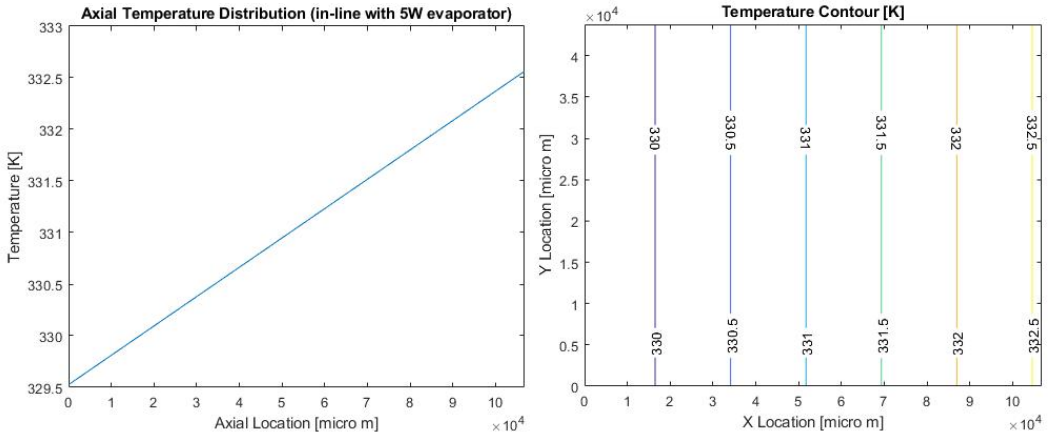

Figure 15 – 1D and 2D temperature profiles: 5W evaporator spanning entire width.

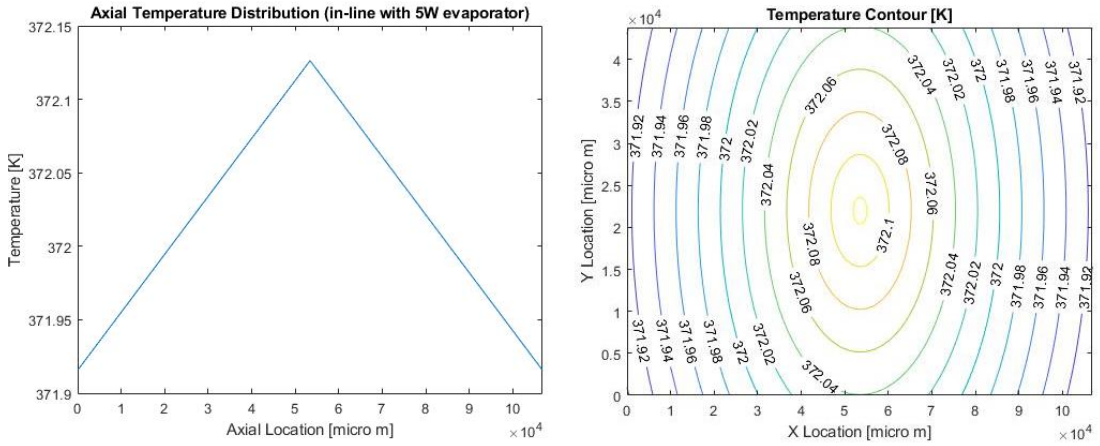

Figure 16 – 1D and 2D temperature profiles: 5W evaporator centered on TGP.

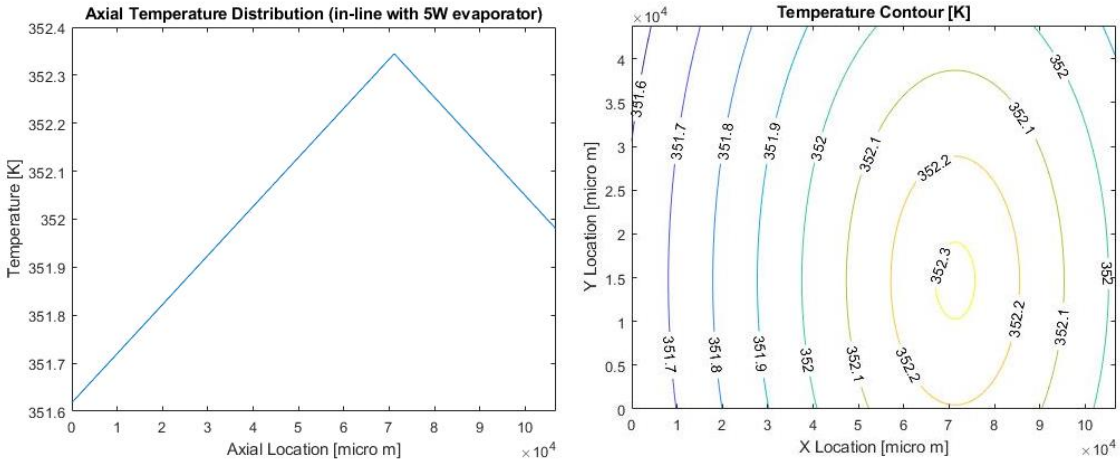

Figure 17 – 1D and 2D temperature profiles: 5W evaporator skewed bottom right.

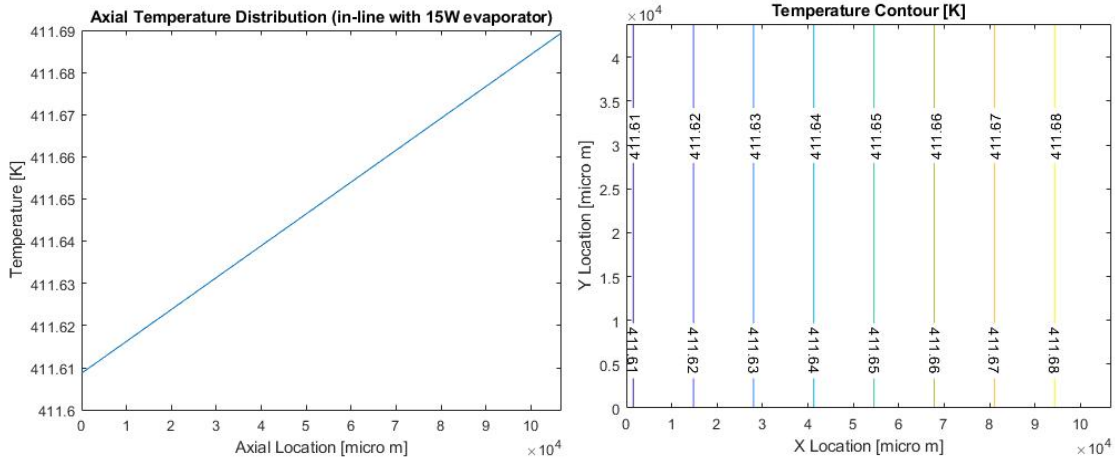

Figure 18 – 1D and 2D temperature profiles: 15W evaporator spanning entire width.

CHAPTER 3. EXPERIMENTAL EXAMINATION

3.1 Test Facility

Testing of various TGPs provides data for design tool updates and determination of accuracy. Lewis et al. [2] conceptualize a “thermal performance apparatus” for TGPs, modified for this application. A similar test facility is applicable to this effort, with some necessary modifications. Figure 19 details the 1D and 2D test setups.

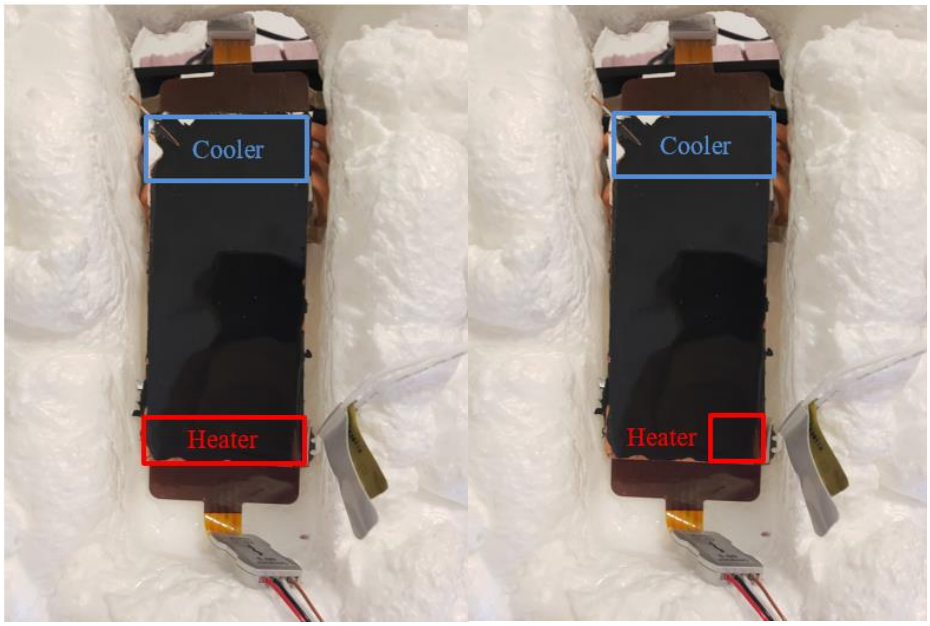

Figure 19 – Test setup. Left: 1D, Right: 2D

The evaporator and condenser sections span the width of the TGP in order to simulate one-dimensional heat transfer. For two dimensional testing, a smaller heater forms a corresponding evaporator section in one corner furthest away from the condenser which spans the TGP width. Foam insulation surrounds the TGP test setup, leaving the CPU cooler open (Figure 20). Vacuum may provide better insulation, but was not an option in this experimental test program.

Figure 20 – Foam insulation setup. Left: Top view, Right: Cooler/back view

3.1.1 Components

The following sections detail each component used in this test setup.

3.1.1.1 Test Articles

Kelvin Thermal provided four TGP test articles with sample numbers: KT1, KT2, GT1, and GT2. These samples have an expected maximum power of about 11W and thermal conductivities between 7,000 and 20,000 W/m·K [6]. Figure 21 provides visuals of the test articles. Although the different sample numbers of KT and GT suggest that the KT samples may differ from GT samples, all samples are 115mm x 52mm x 0.3mm copper-water TGPs with the same geometric specs as shown in Figure 22 through Figure 25.

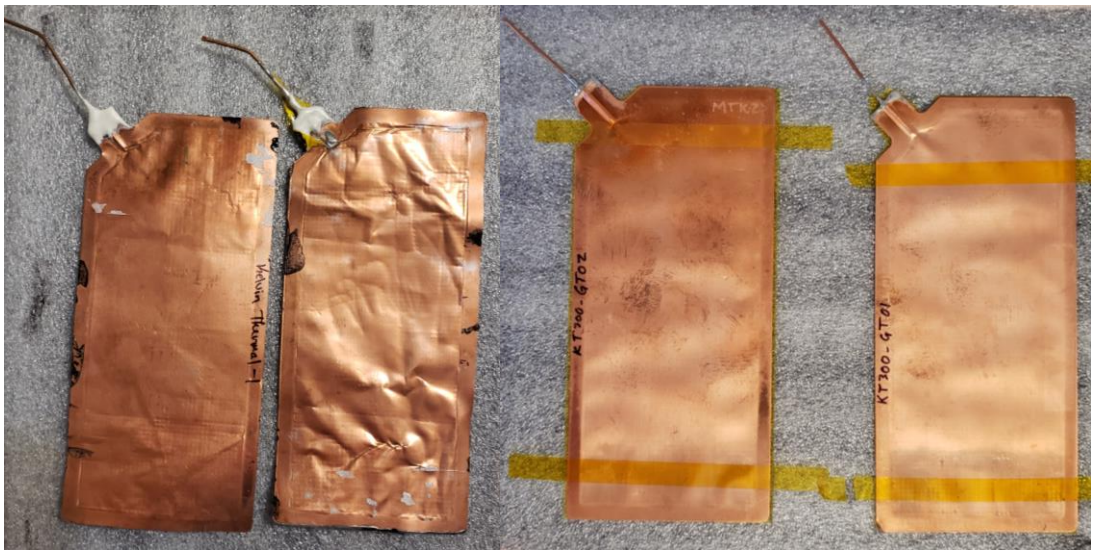

Figure 21 – Test articles. Left: KT samples, Right: GT samples.

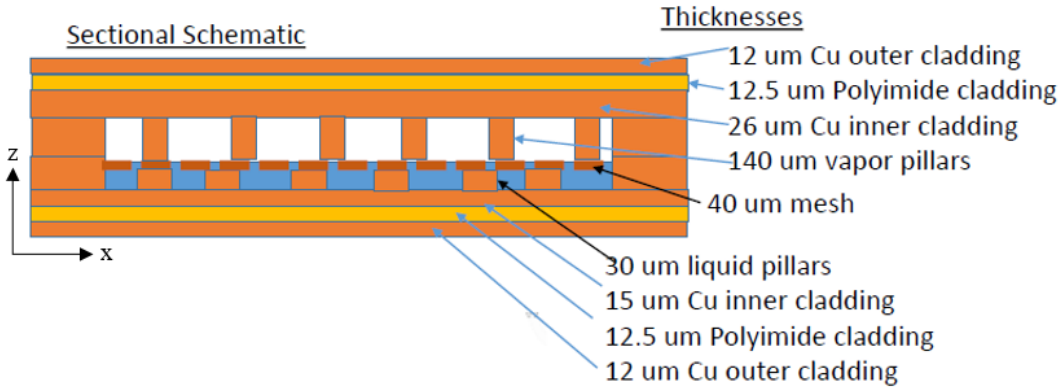

Figure 22 – TGP cross-sectional view.

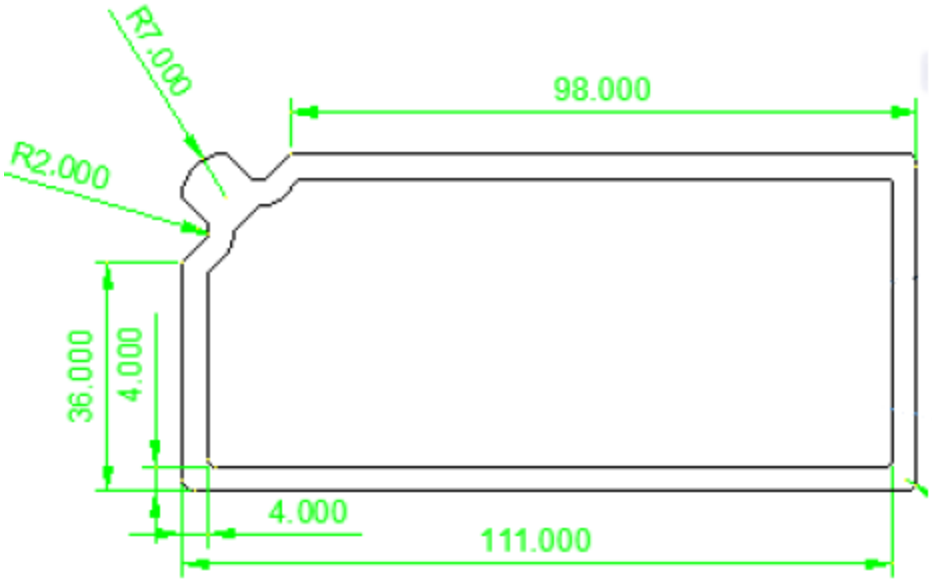

Figure 23 – TGP top dimensions [mm].

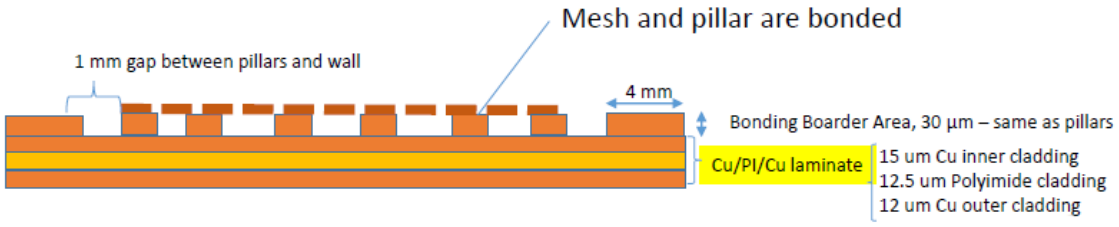

Figure 24 – TGP liquid pillar, mesh, and cladding details.

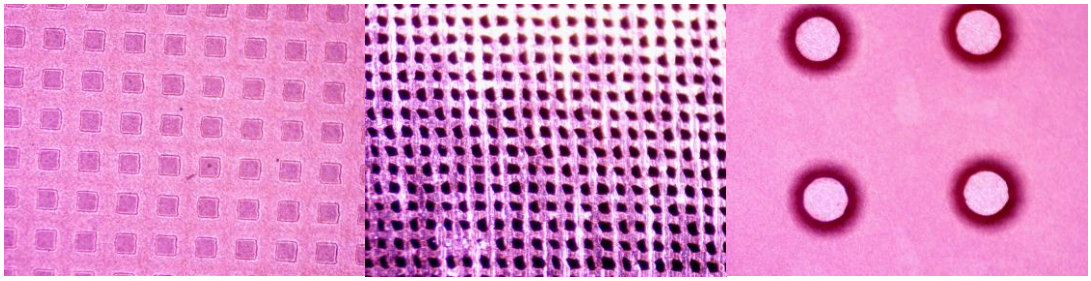

Figure 25 – TGP liquid pillars (left), liquid wick capping mesh (middle), and vapor pillars (right).

Copper and polyimide layers form the 0.0505mm outer cladding, with copper forming the external sides. Liquid pillars bonded with a liquid wick capping mesh create the porous media for fluid flow. The liquid pillars are made up of a square array of squares,

with a width of 0.150mm, spacing of 0.150mm, and height of 0.030±0.003mm. The liquid wick capping mesh is a planar mesh with a thickness of 0.035±0.005mm made from wire with a width of 0.060mm and pore sizes of 0.065mm. The vapor pillars are made up of a square array of cylinders with diameters of 0.30mm to about 0.50mm at the base. Vapor pillars have a center to center pitch of 1.25mm and a height of 0.150±0.005mm.

3.1.1.2 Evaporator

Thin, flexible polyimide heaters produced by Watlow, create the evaporator section of the TGP (Figure 26). Thermal tape with a thermal conductivity greater than 3.17 W/m·K adheres the heater to the TGP, with a flux sensor in between to measure actual flux (Figure 27).

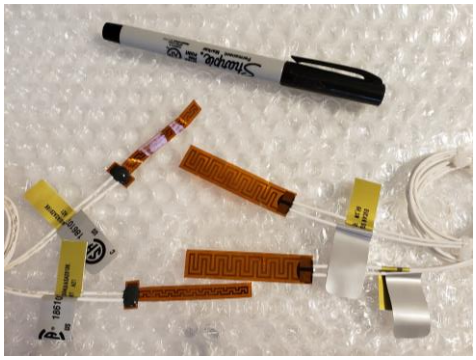

Figure 26 – Flexible polyimide heaters.

Figure 27 – Application of heater to flux sensor and flux sensor to TGP.

Varying the sizes and wattages of these heaters provides various heat loads and thermal responses. Kelvin Thermal quotes a maximum TGP load capability of 11W, so testing uses wattage values below this limit. One-dimensional testing applies a theoretical heat load of 6W with a 0.5 inch by 2 inch heater. A smaller heater size with dimensions 0.25 inch by 0.5 inch provides the two-dimensional thermal response. Due to resistance limitations within heater production, these smaller evaporator sizes provide smaller heat loads of 3W. Heater sizes correspond directly to theoretical evaporator size applied in testing.

3.1.1.3 Condenser

A simple CPU heat sink is used to monitor the conditions in the condenser section (Figure 28). Thermal tape connects the heat sink and TGP with a flux sensor in between, similar to the heater setup.

Figure 28 – CPU cooler heat sink.

CPU cooler capabilities far surpass the small heat load values used in testing, so the CPU cooler alone successfully cools the system. Similar to the heater application for 1D testing, the CPU cooler spans the entire TGP width and creates an evaporator section corresponding to its contact area.

3.1.1.4 Measurements

Lewis et al. [2] used thermocouples within the heat sink material to measure condenser heat flux. The low power values used in this application require an unrealistic cross-sectional area and/or a large distance between thermocouples to measure heat flux in this way. Instead, heat flux sensors provide flux measurements for both the condenser and the evaporator sections (Figure 29).

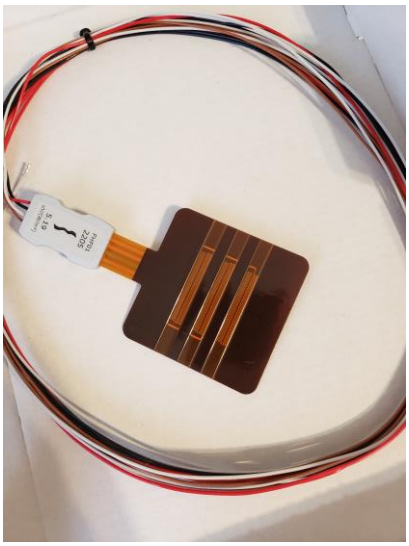

Figure 29 – Heat flux sensor.

Hukseflux manufactures two types of these sensors. One provides more accurate measurements, but includes an aluminum foil spreader in order to obtain this accuracy. Although the aluminum foil spreader layer may not skew results, if the evaporator and condenser are modeled as uniform, the other less accurate sensor does not force this uniform model assumption. The difference in flux between the evaporator and condenser provides the most important parameter measured by these sensors. Using the same type of sensor on both the evaporator and condenser minimizes the accuracy issue by taking a difference between measurements. Therefore, the sensor without the aluminum foil spreader provides flux readings for this effort.

These flux sensors also provide temperature measurements with T-type thermocouples. These thermocouples have an accuracy of ±1˚C. Similar to the flux reading argument, the difference in temperature across the TGP provides the most applicable information. Using the same heat flux sensors in each application provides comparable data between each case, with a ±2˚C uncertainty.

Calibration uncertainty of these flux sensors is quoted as <±5%. Re-calibration is required every two years. Although these sensors are less than two-years old, a small calibration experiment provides information about flux sensor measurement accuracy. A 0.25in by 2in, 6V, 3W heater provides a well characterized heat load to the flux sensor with the following equation.

$$Expected\ Flux = \frac{Wattage\ Povided}{Area} \tag{43}$$

The wattage provided, measured from the power source, has an uncertainty of <0.01% + 3mV and <0.2% + 3mA. The expected flux error introduced by these uncertainties is 2e-5 W/m^2, an extremely small value compared to flux measurements, and is noted here rather than in the table. Measurements are taken from the flux sensor in volts and converted to flux with the sensor sensitivity (5.19e-6) by the following equation.

$$Flux\ \left[\frac{W}{m^2}\right] = \frac{Voltage\ Output\ [V]}{Sensitivity\ \left[\frac{V}{W/m\hat{}2}\right]} \tag{44}$$

Table 3 compares measured and expected flux readings with their corresponding uncertainties.

Table 3 – Measured and expected flux comparison [W/m^2].

Measured Flux	Expected Flux	% Difference
3600±200	3765.18	10
3600±200	3765.18	10
3600±200	3765.18	10

A FLIR One camera also provides temperature difference across the TGP (Figure 30). This portable camera interfaces with an IPhone app. A jet black paint applied to the top surface of the TGP provides a clear surface for the FLIR to read. As the same tool provides all temperature data, the FLIR provides a clear measurement for temperature difference across the TGP. FLIR uncertainty is the larger of ±3˚C or ±5%. This FLIR camera provides general emissivity settings rather than allowing the user to set exact emissivity of the surface, skewing absolute temperature results. Comparison of FLIR temperature readings and thermocouple readings at the same location provide calibration of the FLIR One camera. Section 4.1 discusses this emissivity setting and how the results account for it in more detail.

Figure 30 – FLIR One device.

3.2 Methods

Execution of testing methods begins with noting: date and start times, heater specs, heater location, and flux sensor specs for both the evaporator and condenser sections. The power source then provides power to the heater, set to the correct voltage and amperage values corresponding to the heater used. At time intervals of one hour, the following measurements are recorded:

1. Actual voltage (uncertainty of <0.01% + 3mV) and amperage (uncertainty of <0.2% + 3mA) values as measured from the power source
2. Room air temperature measured with K-type thermocouple (uncertainty the larger of ±2.2 ˚C or ±0.75%)
3. Evaporator temperature (uncertainty ±1˚C) and flux (uncertainty <±5%) measured by the heater flux sensor
4. Condenser temperature (uncertainty ±1˚C) and flux (uncertainty <±5%) measured by the condenser flux sensor
5. Evaporator and condenser temperatures measured at the top surface of the TGP with K-type thermocouples (uncertainty the larger of ±2.2 ˚C or ±0.75%)
6. FLIR image (uncertainty the larger of ±3˚C or ±5%)

Between the time intervals of three to four hours, both the condenser and evaporator temperatures change less than 1% (0.6% and 0.3% respectively). Assuming steady-state after four hours from the start time, three data sets as described above were recorded. Repetition of this process for each TGP in both 1D and 2D configurations provides a repeatable dataset used for design tool comparison.

With three sets of measurements, comparison between design tool data and recorded data often uses average temperature and flux values. The below equation for standard uncertainty provides error results for average values [10].

$$SU = \frac{s}{\sqrt{N}} \tag{45}$$

With the number of measurements (N) and the standard deviation (s) calculated using the uncertainty of each measurement (δx) as follows.

$$s = \sqrt{\frac{\delta x_1^2 + \delta x_2^2 + \delta x_3^2}{N-1}} \tag{46}$$

Measured data with corresponding uncertainties is used to calculate various parameters such as thermal conductivity. In the case of thermal conductivity, these measurements include the heat load and temperature difference. The law of propagation of uncertainty computes the error introduced into these calculations as follows [10].

$$\delta(f) = \sqrt{\left(\frac{\partial f}{\partial x_1}\right)^2 \delta(x_1)^2 + \left(\frac{\partial f}{\partial x_2}\right)^2 \delta(x_2)^2 + \cdots + 2\frac{\partial f}{\partial x_1}\frac{\partial f}{\partial x_2}\delta(x_1, x_2) + \cdots} \tag{47}$$

With the uncertainty of the calculated parameter ($\delta(f)$), the measurements (x) which the function depends on, and their corresponding uncertainties ($\delta(x)$).

An experiment using solid copper provides method verification and equipment calibration. The above experimental methods were executed in a 1D fashion using a 3V 6W heater with dimensions 0.5in by 2in and a solid copper piece with dimensions 4.5in by 2.125in. Table 4 provides a comparison of the measured thermal conductivity using FLIR and flux sensor measurements and actual copper thermal conductivity.

Table 4 – Comparison of measured and actual copper thermal conductivity [W/m·K].

Actual	Measured	
	FLIR	Flux Sensor
397	423.1	358.5

The two measurement methods bound the actual thermal conductivity on both sides with FLIR temperatures overestimating thermal conductivity and flux sensor temperatures underestimating thermal conductivity. The average difference is 32.3 W/m·K or 8.1%. The

FLIR measures a temperature difference across the copper of 11.1°C and the flux sensor measures this difference as 13.1°C. With a small heat load of 0.7W this small difference of 2°C between measurement methods greatly impacts thermal conductivity results. It is then important to note that the impact of small temperature differences and measurement errors may have large impacts on measured thermal conductivity calculations during TGP testing. In retrospect had this calibration test occurred earlier in the testing process, stronger heaters may have provided larger heat loads minimizing this temperature effect. Longer heaters, with filament surface areas spanning larger than the entire copper width, may have also provided a larger heat load with minimal losses to the environment from the sides.

CHAPTER 4. RESULTS AND DESIGN TOOL COMPARISON

4.1 Design Tool Comparison

Comparing results from both 1D and 2D testing to the analytical design tool provides insight into the accuracy and any necessary updates the tool may require.

4.1.1 One-Dimensional

Measured thermal conductivity, an important TGP parameter, is calculated using the following equation which varies with temperature difference across the TGP as well as heat load.

$$\lambda_{measured} = \frac{LQ}{A\Delta T} \tag{48}$$

Comparing the recorded temperature difference from each method helps decide which measurements to use to evaluate design tool accuracy. If both methods provide similar measurements one may be chosen for comparison, but if the methods provide different measurements, results from both methods are required for a thorough comparison. Table 5 provides average temperature difference across the TGP surface, recorded from both FLIR images and flux sensors during 1D testing. Both heat flux sensors and FLIR images record the temperature difference.

Table 5 – Average temperature difference across TGP samples [˚C].

Sample	FLIR ΔT	Flux Sensor ΔT
KT1	28.7±4.5	23.7±1.4
KT2	44.9±5.0	32.7±1.4
GT1	6.8±4.2	17.4±1.4
GT2	8.1±4.2	20.1±1.4

The temperature difference measured by the FLIR and heat flux sensor differ by a maximum value of 18.6˚C. Due to this difference, results from both methods are compared to design tool results rather than one method, for an exhaustive approach.

Figure 31 provides one FLIR image for each sample taken during 1D testing at steady-state conditions.

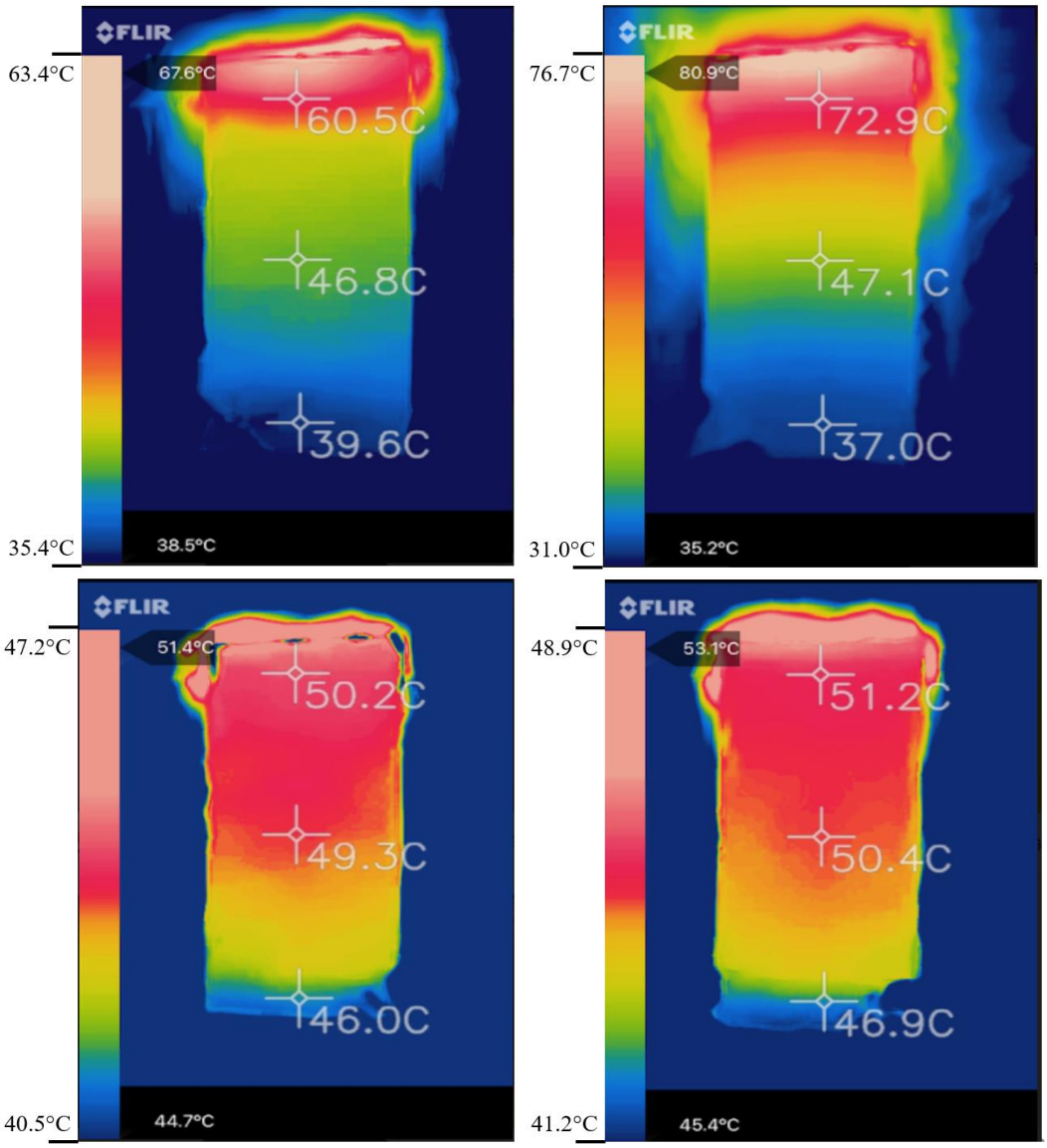

Figure 31 – FLIR images from 1D steady-state testing. Top left: KT1, Top Right: KT2, Bottom Left: GT1, Bottom Right: GT2

Overall, modeled contours correlate well to FLIR measured contours, with both showing rough 1D temperature profiles across the TGP. Temperature varies though, with FLIR measuring larger temperatures than those predicted by the design tool. This may be due to the FLIR's extremely general emissivity setting options, set to "Matte", differing from the actual TGP emissivity. Comparison of FLIR temperature readings and

thermocouple readings at the same location provide adjustment factors to account for this general emissivity setting. Although the actual emissivity shift calculation may depend on surface temperature, using a ratio of setting emissivity to the known emissivity, a general emissivity shift factor provides a valid estimation due to the small difference in temperatures across the system. Adjusted maximum and minimum temperature values, adjusted for emissivity in this way, accompany each FLIR image to the left of the FLIR scale. Although absolute temperature values differ between modeled and measured results, thermal conductivity calculations use the difference in temperature across the TGP as shown in Equation (48) rather than the absolute temperature values. This temperature difference across the TGP varies by an average of 2.09˚C between modeled and measured results.

Figure 32 compares temperature contour data from FLIR, adjusted FLIR, and heat flux sensors to theoretical design tool results with a one dimensional contour assumption. The tool uses an average of condenser and evaporator flux sensor readings for heat load input which introduces a standard error of ±9.35e-5 W, or .012% of the input value. This accounts for some practical flux losses, as the system did have insulation but was not in perfect vacuum, and should provide the best direct temperature comparison. Considering Equation 33, and making use of the propagation of uncertainty analysis (Equation 47), this introduces an uncertainty to the design tool's calculated ΔT of ±9.35e-5·R˚C. On average, this introduces an uncertainty of 2.5-4˚C. Due to this small uncertainty value compared to the temperature scale of the plots, Figure 32 forgoes error bars on the design tool temperature values, and instead notes this uncertainty in the text.

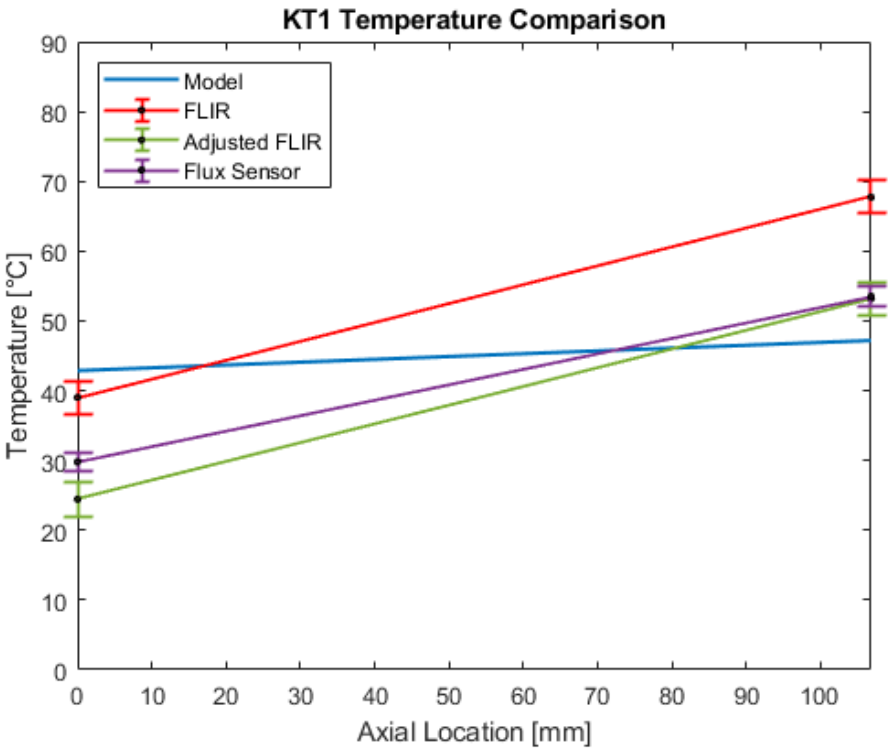
KT1 Temperature Comparison
Model
FLIR
Adjusted FLIR
Flux Sensor
Temperature [°C]
Axial Location [mm]
0
10
20
30
40
50
60
70
80
90
100

(32a)

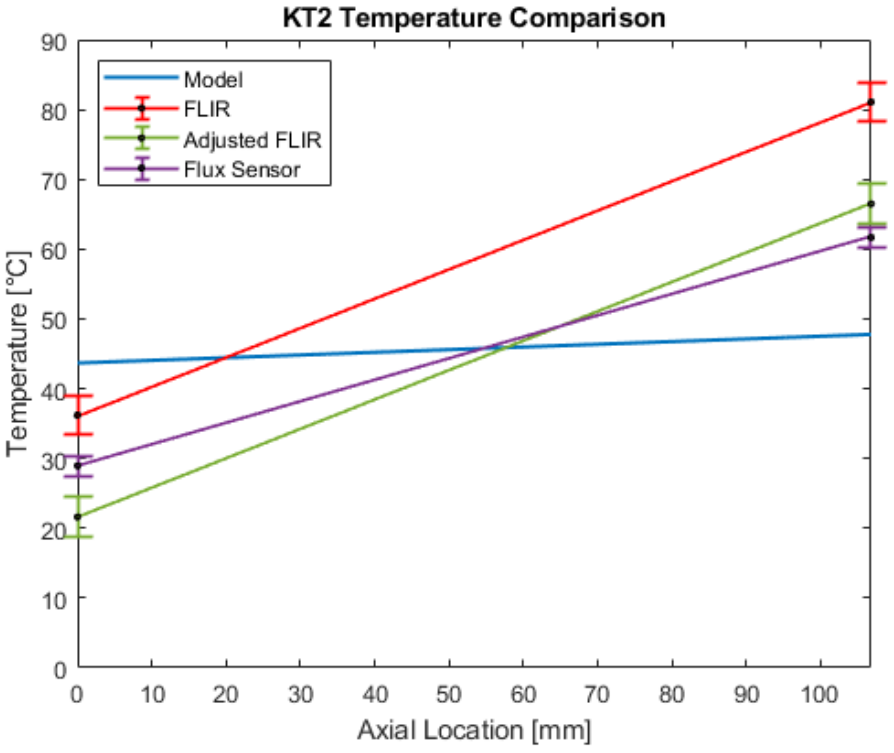
KT2 Temperature Comparison
Model
FLIR
Adjusted FLIR
Flux Sensor
Temperature [°C]
Axial Location [mm]
0
10
20
30
40
50
60
70
80
90
100

(32b)

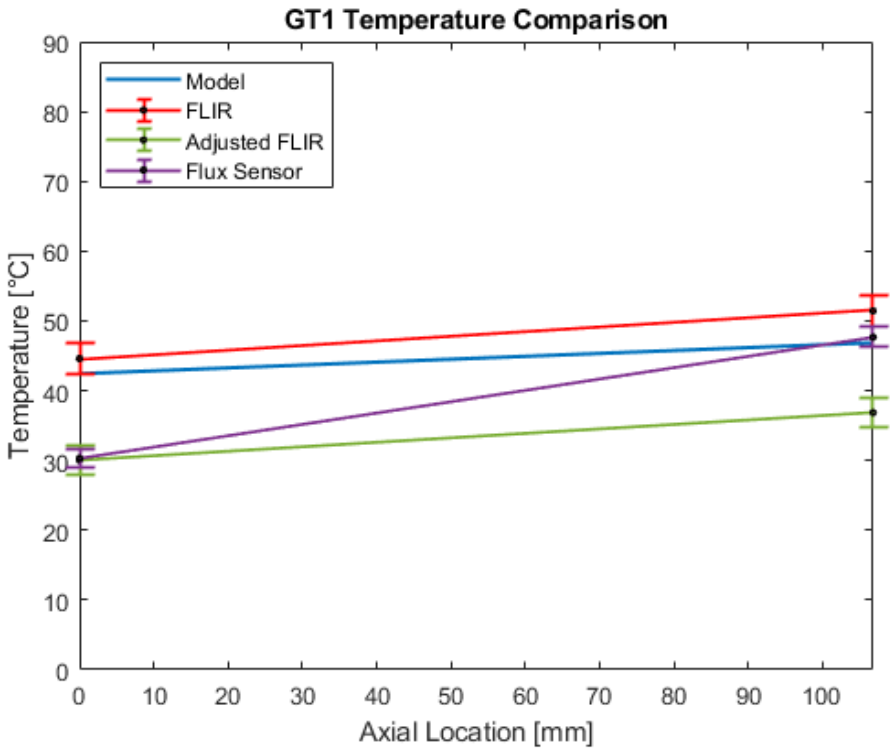

(32c)

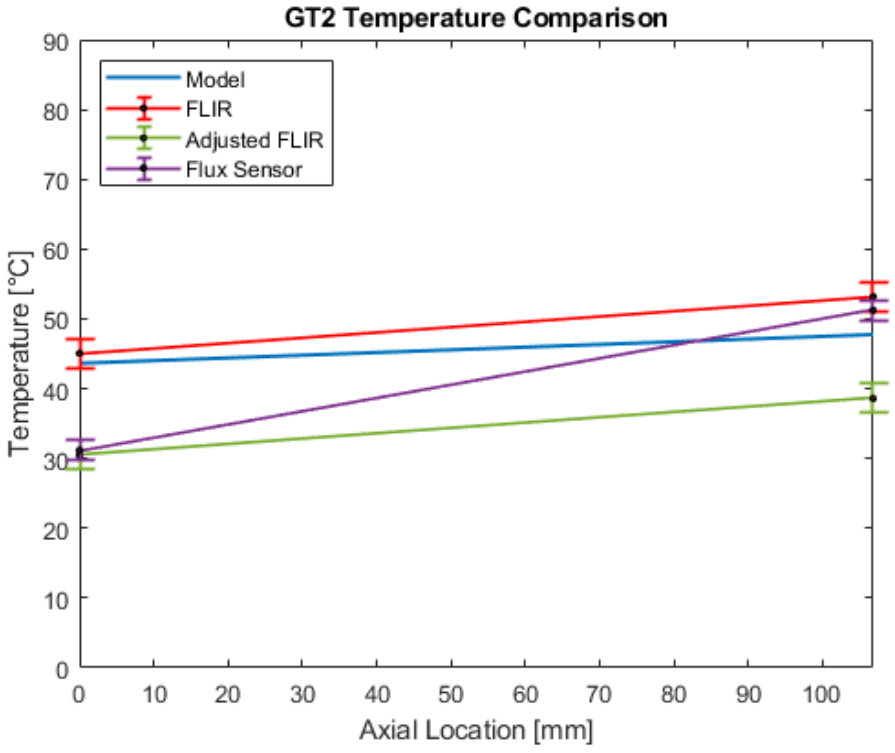

(32d)

Figure 32 – Temperature comparison between 1D steady-state measured and design tool results. 32a: KT1, 32b: KT2, 32c: GT1, 32d: GT2

Table 6 provides thermal conductivity comparison between theoretical calculations and measured values. Equation 48 calculates measured thermal conductivity using temperature difference across the TGP taken with both FLIR and heat flux sensors. Propagation of uncertainty analysis (Equation 47) provides error values. High FLIR thermal conductivity uncertainty values are due to the temperature difference uncertainty contribution. When ΔT across the TGP is small, a small denominator value in the uncertainty calculation causes a large overall uncertainty.

Table 6 – 1D thermal conductivity comparison [W/m·K].

Sample	Design Tool	Measured	
		FLIR	Flux Sensor
KT1	8385.7±0.2	631.0±10.0	764.1±8.7
KT2	8807.7±0.2	402.7±5.6	551.9±5.2
GT1	8169.5±0.2	2656.1±171.9	1045.1±17.8
GT2	8793.3±0.2	2226.5±153.8	902.4±16.9

The purely theoretical model, prior to any adjustments, underestimates absolute temperature and over-estimates TGP thermal conductivity. Section 4.2 suggests possible thermal conductivity and absolute temperature adjustments for the user wishing to calculate actual values rather than theoretical.

4.1.2 Two-Dimensional

One dimensional testing caused separation between the mesh and liquid pillars to occur in the Kelvin Thermal samples. Therefore, the GT samples are used for 2D testing. Figure 33 provides visual comparison between modeled and FLIR temperature contours from 2D testing. Similar to 1D testing, the tool uses an average flux value as discussed in the previous section.

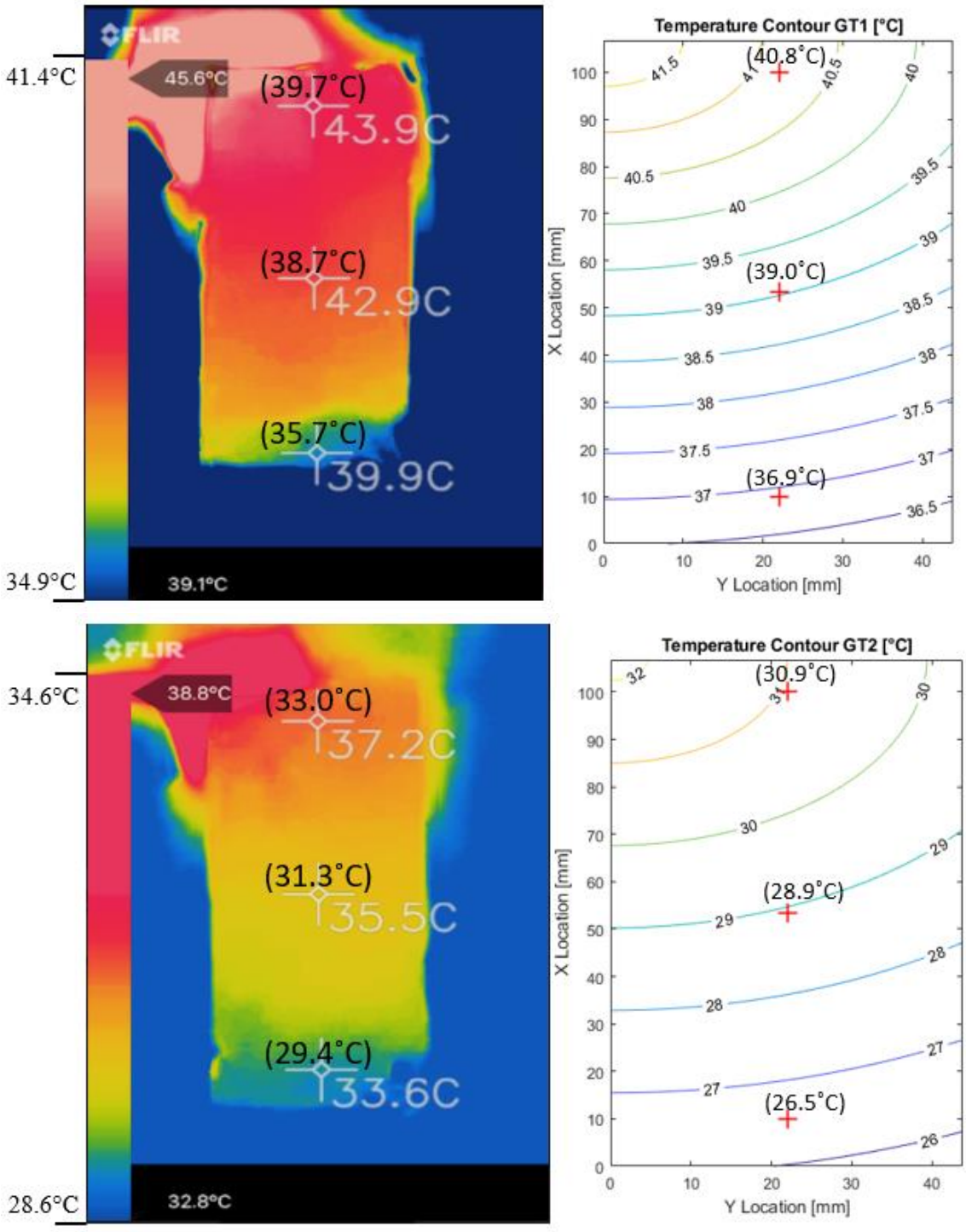

Figure 33 – FLIR images from 2D steady-state testing compared with design tool temperature contours. Top left: GT1 FLIR, Top Right: GT1 Modeled Contour, Bottom Left: GT2 FLIR, Bottom Right: GT2 Modeled Contour

Both FLIR and design tool temperature contours show radial heat distribution around the evaporator location (top left) which becomes more linear as it reaches the condenser section (bottom). A lesser heat load was applied to GT2 because the small heater melted at the end of testing GT1 due to a high heat flux input. For this reason, GT2 presents a cooler temperature distribution. Temperature difference across the TGP provides the most important data for thermal conductivity calculations. Table 7 compares modeled and measured values for this overall temperature difference.

Table 7 – Temperature difference comparison across TGP [˚C].

Sample	FLIR ΔT	Modeled ΔT	Over/Underestimation
GT1	6.5±1.4	5.5±0.001	-2.4
GT2	5.7±1.4	6.2±0.001	1.9

Figure 34 directly compares measured and modeled 1D axial temperature profiles in-line with the evaporator center. Section 0 details the modeling methods of this 1D profile. Table 8 provides predicted and measured thermal conductivity comparisons for both samples.

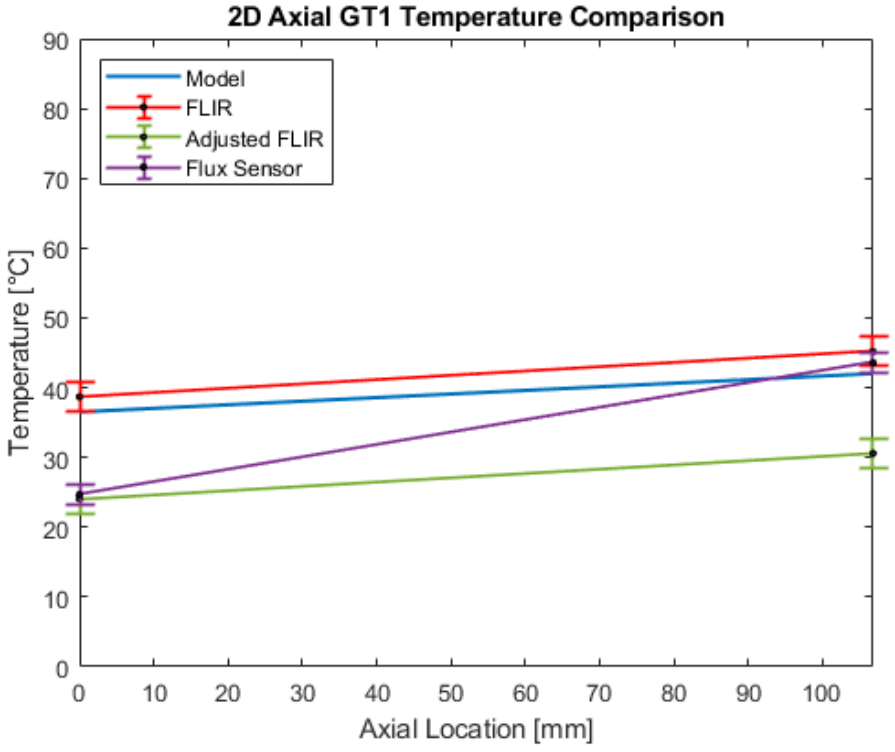

(34a)

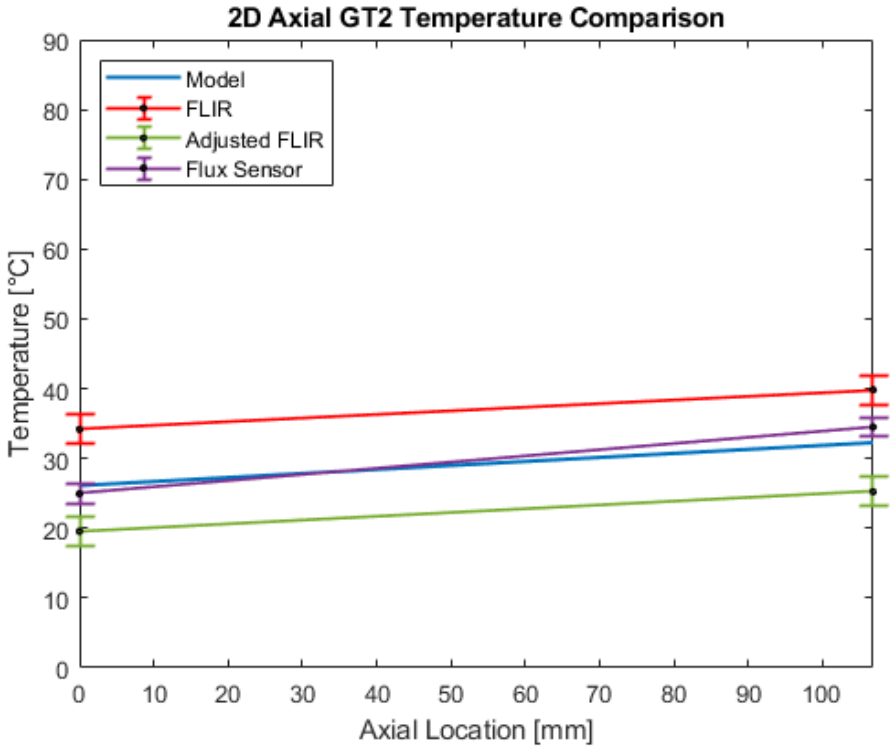

(34b)

Figure 34 – 1D axial temperature profile comparison in line with evaporator of 2D testing. 34a: GT1, 34b: GT2

Table 8 – 2D thermal conductivity comparison [W/m·K].

Sample	Design Tool	Measured	
		FLIR	Flux Sensor
GT1	5374.4±0.1	2272.5±110.8	781.6±8.8
GT2	2288.2±0.1	1242.7±56.1	736.1±13.1

Similar to the 1D case, the theoretical model estimates larger conductivities than actual values. The next section addresses this, and provides some suggested design tool adjustments to better estimate practical responses.

4.2 Design Tool Adjustments

Overall, theoretical design tool calculations overestimate TGP conductivities and underestimate absolute temperature. Theoretical models provide best-case calculations, but losses do occur during testing which minimize actual thermal conductivity values and increase temperatures. These losses include heat loss from the top of the TGP and frictional losses from fluid and vapor flows. Along with practical losses, various assumptions within the model simplify the internal physics, calculating a best estimate of actual parameters. One such assumption made in this design tool is neglecting the pressure drop at the phase transition since it is small compared to other pressure drops. These assumptions may be updated if necessary, as study in the field progresses. Calibration of flux sensors also provided an average measured flux uncertainty of 10%. The design tool uses measured flux as an important input to calculate results, which may be over or under-estimated by this 10% causing some discrepancies between design tool and measured results.

Design tools provide functionality in multiple ways. As previously established, one use is to provide theoretical, best-case estimations of important parameters. Another usage is to calculate parameters while accounting for practical losses and the impact of various

assumptions within the model. To provide these calculations, theoretical results are shifted by a correction factor to correlate better with measured data. Correction factors provide analysts with the ability to calculate more accurate thermal conductivity and temperature profiles alongside theoretical values. As more data becomes available, these correction factors become more accurate and the design tool provides better estimates for these parameters. While the tool retains the ability to estimate theoretical best-case values, these correction factors provide extra functionality by fine-tuning calculated results to correlate with measured results. Sections 4.2.1 and 4.2.2 detail these correction factors and their suggested usage.

4.2.1 Thermal conductivity

Theoretical design tool calculations consistently overestimate TGP conductivities. A thermal conductivity adjustment provides functionality to users wishing to calculate a thermal conductivity that accounts for losses and assumptions. A thermal conductivity adjustment input provides this capability. The suggested adjustment factor is calculated using the following equation.

$$Conductivity\ Adjustment\ Factor = \frac{Average\ Estimated\ Conductivity}{Average\ Measured\ Conductivity} \tag{49}$$

An adjustment factor of 0.18 shifts the design tool thermal conductivity to better correlate with measured results. Setting the variable *cond_adjustment* equal to this adjustment factor provides the user with an adjusted thermal conductivity value *k_TGP_sensible* in [W/m·K].

Using these adjustment factors, Figure 35 and Table 9 provide updated design tool comparisons with measured data.

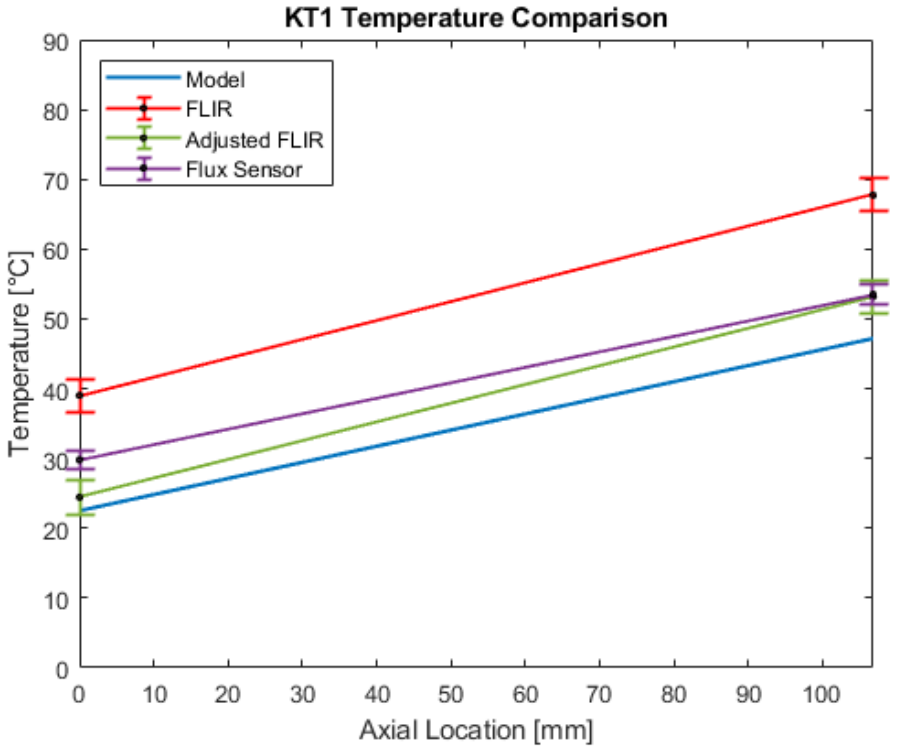

(35a)

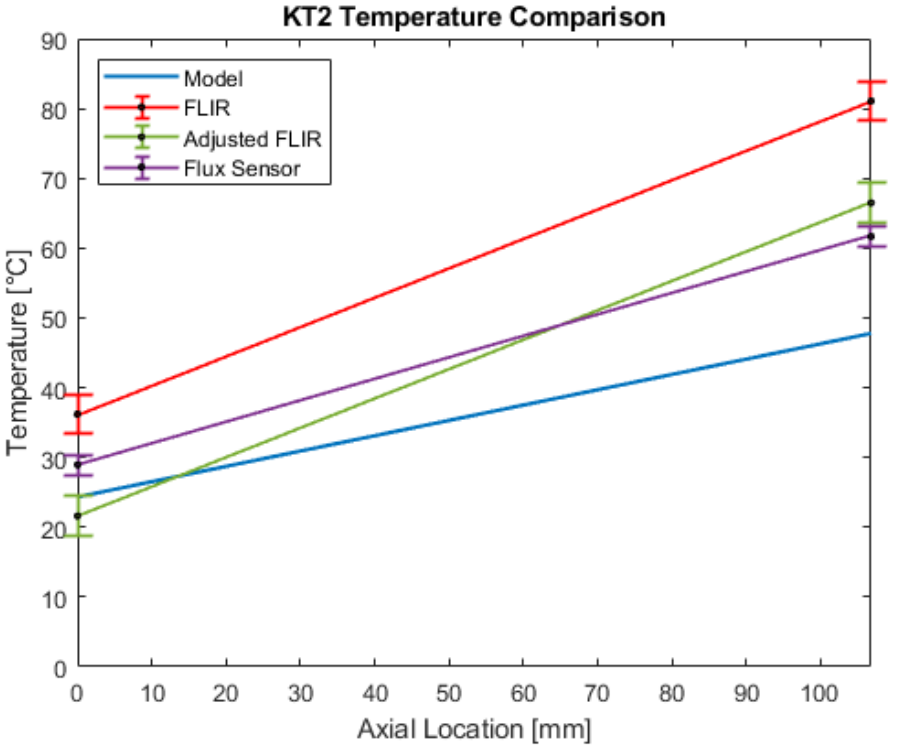
KT2 Temperature Comparison
Model
FLIR
Adjusted FLIR
Flux Sensor
Temperature [°C]
Axial Location [mm]
0
10
20
30
40
50
60
70
80
90
100

(35b)

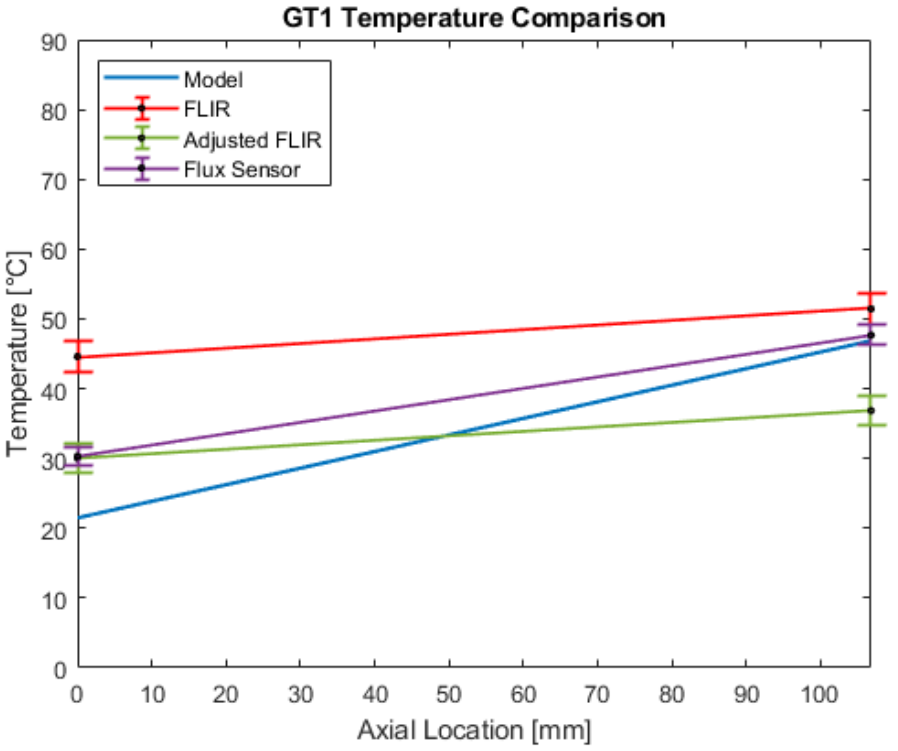
GT1 Temperature Comparison
Model
FLIR
Adjusted FLIR
Flux Sensor
Temperature [°C]
Axial Location [mm]
0
10
20
30
40
50
60
70
80
90
100

(35c)

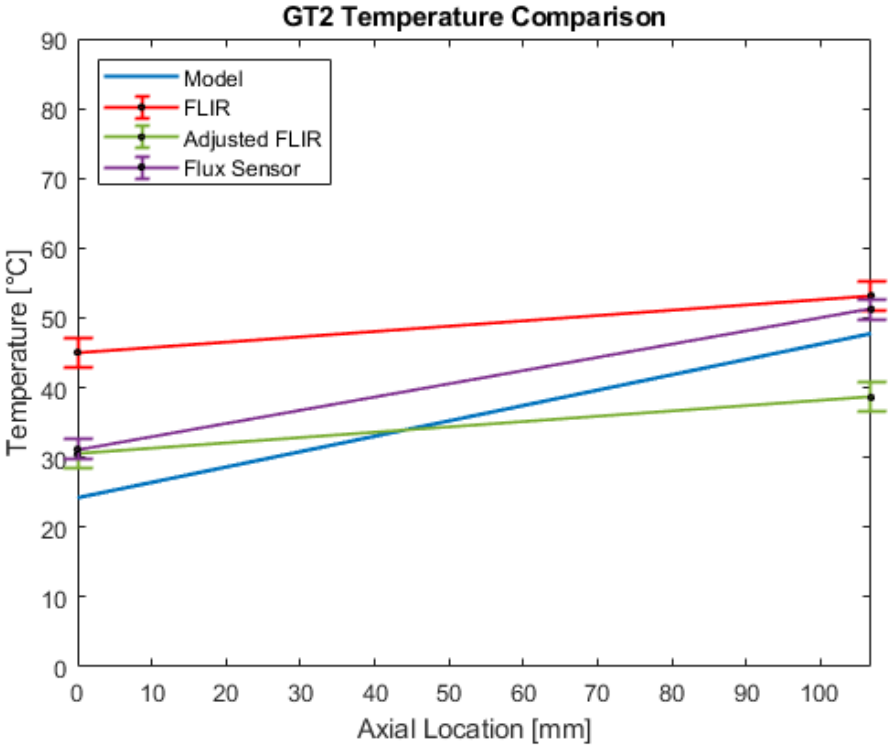
GT2 Temperature Comparison
Model
FLIR
Adjusted FLIR
Flux Sensor
Temperature [°C]
Axial Location [mm]
0
10
20
30
40
50
60
70
80
90
100

(35d)

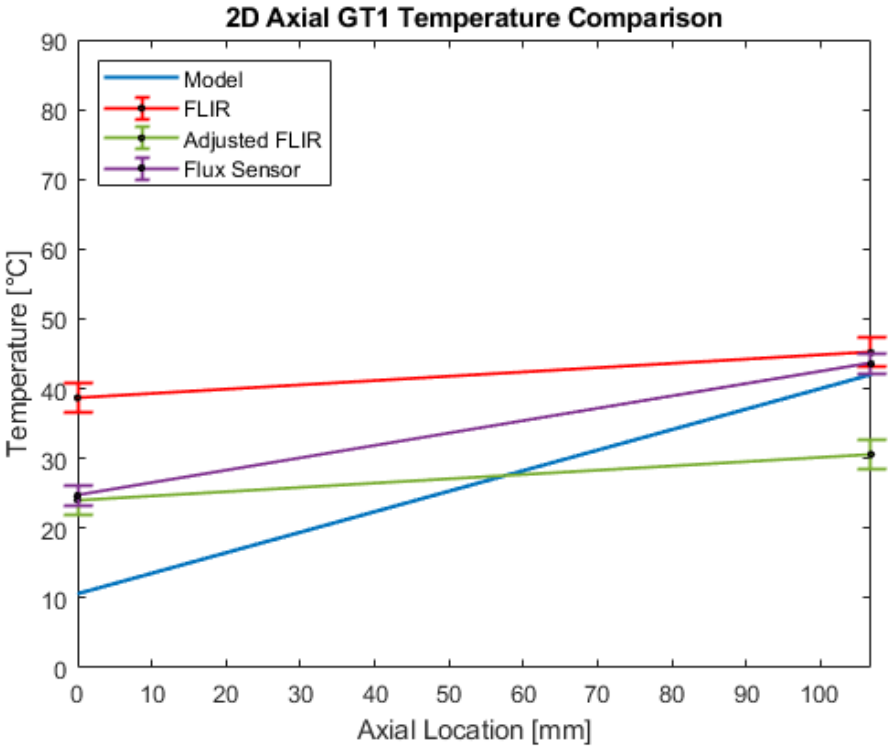
2D Axial GT1 Temperature Comparison
Model
FLIR
Adjusted FLIR
Flux Sensor
Temperature [°C]
Axial Location [mm]
0
10
20
30
40
50
60
70
80
90
100

(35e)

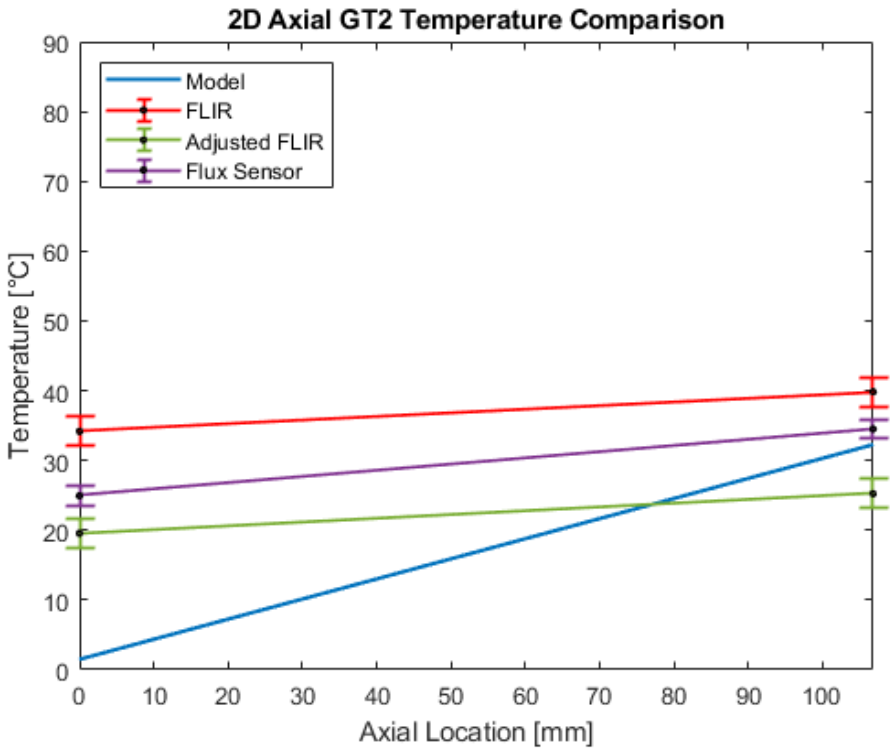

(35f)

Figure 35 – Updated temperature comparison between 1D and 2D steady-state measured and design tool results. 35a: 1D KT1, 35b: 1D KT2, 35c: 1D GT1, 35d: 1D GT2, 35e: 2D GT1, 35f: 2D GT2

Table 9 – Updated thermal conductivity comparison [W/m·K].

Type	Sample	Design Tool	Measured	
			FLIR	Flux Sensor
1D	KT1	1467.5±0.03	631.0±10.0	764.1±8.7
	KT2	1541.3±0.03	402.7±5.6	551.9±5.2
	GT1	1429.7±0.03	2656.1±171.9	1045.1±17.8
	GT2	1538.8±0.03	2226.5±153.8	902.4±16.9
2D	GT1	940.5±0.03	2272.5±110.8	781.6±8.8
	GT2	400.4±0.03	1242.7±56.1	736.1±13.1

Shifted thermal conductivity values provide more accurate estimates of measured conductivities, correlating well to measured results. Prior to shifting, the theoretical design tool overestimated thermal conductivity on average by 5785.4 W/m·K. After shifting the thermal conductivity this difference becomes 44.9 W/m·K (3.7%) on average.

4.2.2 Temperature

Although thermal conductivity typically provides the most pertinent information, the design tool also includes a temperature correction factor. This shifts temperature calculations to better correlate with measured results. Compared to measured data, the theoretical tool underestimates overall temperature by an average of 5.6˚C. The smaller heat load from 2D testing leads to a lesser overall temperature difference than 1D testing, so Table 10 contains suggested temperature correction factors for both 1D and 2D calculations. A parameter *temp_adjustment* provides the ability to shift this temperature. Shifting overall temperatures the average underestimation amount, Figure 36 provides plots of the updated design tool results compared to measured data.

Table 10 – Suggested temperature adjustment factors [˚C].

Measured	Temperature Adjustment Factor
1D	4.4
2D	6.7

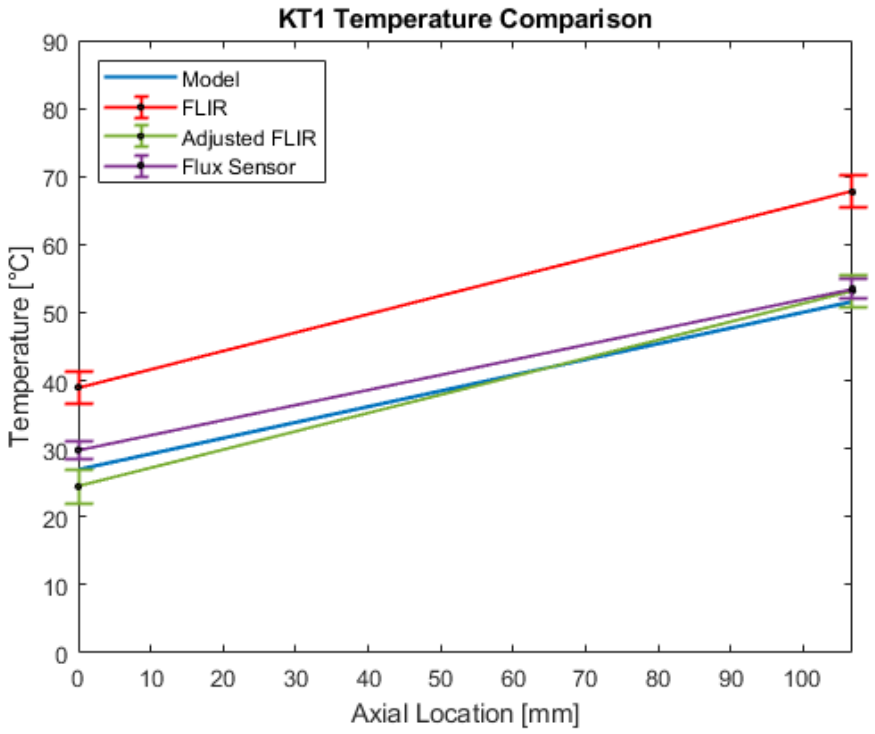
KT1 Temperature Comparison
Model
FLIR
Adjusted FLIR
Flux Sensor
Temperature [°C]
Axial Location [mm]
0
10
20
30
40
50
60
70
80
90
100

(36a)

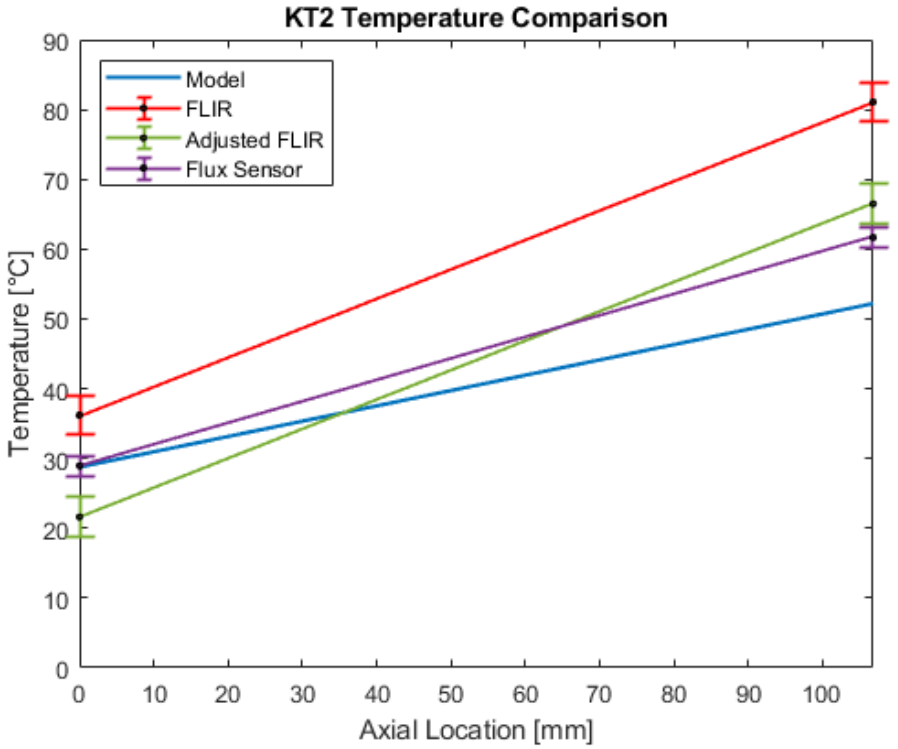
KT2 Temperature Comparison
Model
FLIR
Adjusted FLIR
Flux Sensor
Temperature [°C]
Axial Location [mm]
0
10
20
30
40
50
60
70
80
90
100

(36b)

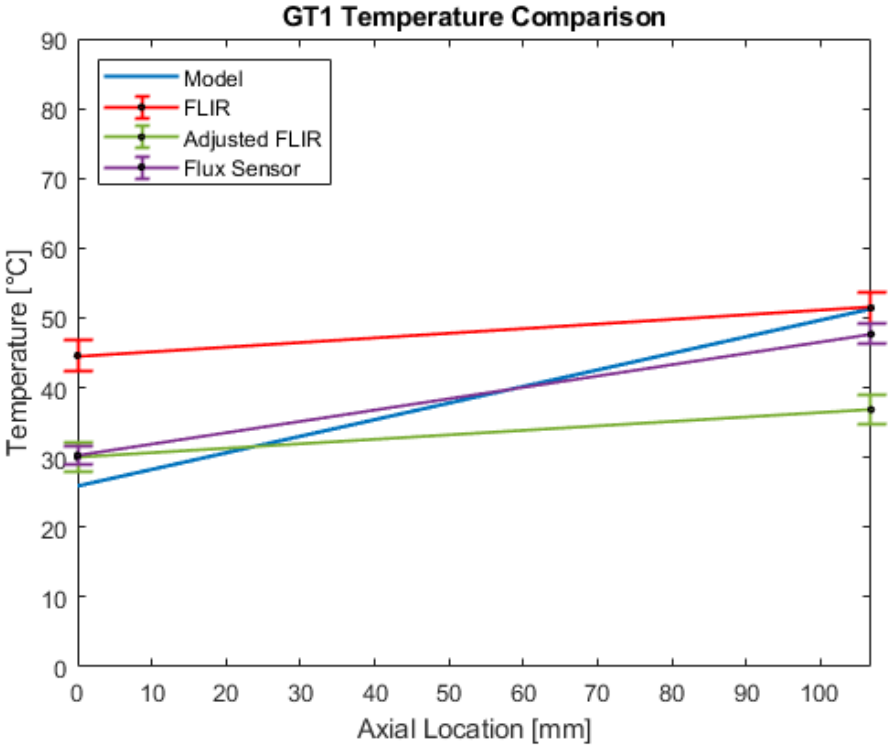
GT1 Temperature Comparison
Model
FLIR
Adjusted FLIR
Flux Sensor
Temperature [°C]
Axial Location [mm]
0
10
20
30
40
50
60
70
80
90
100

(36c)

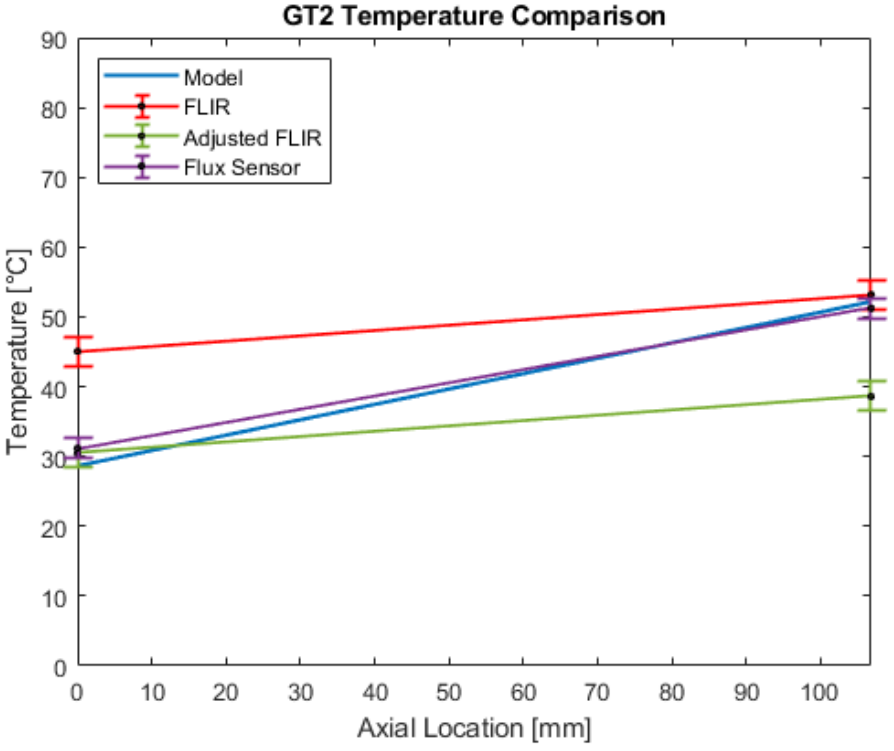
GT2 Temperature Comparison
Model
FLIR
Adjusted FLIR
Flux Sensor
Temperature [°C]
Axial Location [mm]
0
10
20
30
40
50
60
70
80
90
100

(36d)

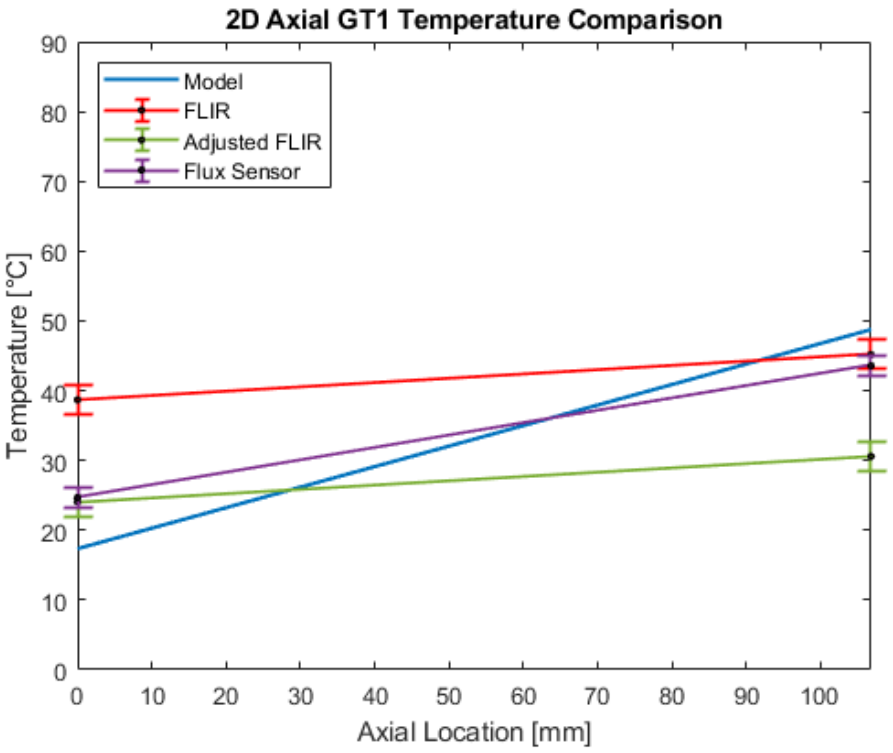
2D Axial GT1 Temperature Comparison
Model
FLIR
Adjusted FLIR
Flux Sensor
Temperature [°C]
Axial Location [mm]
0
10
20
30
40
50
60
70
80
90
100

(36e)

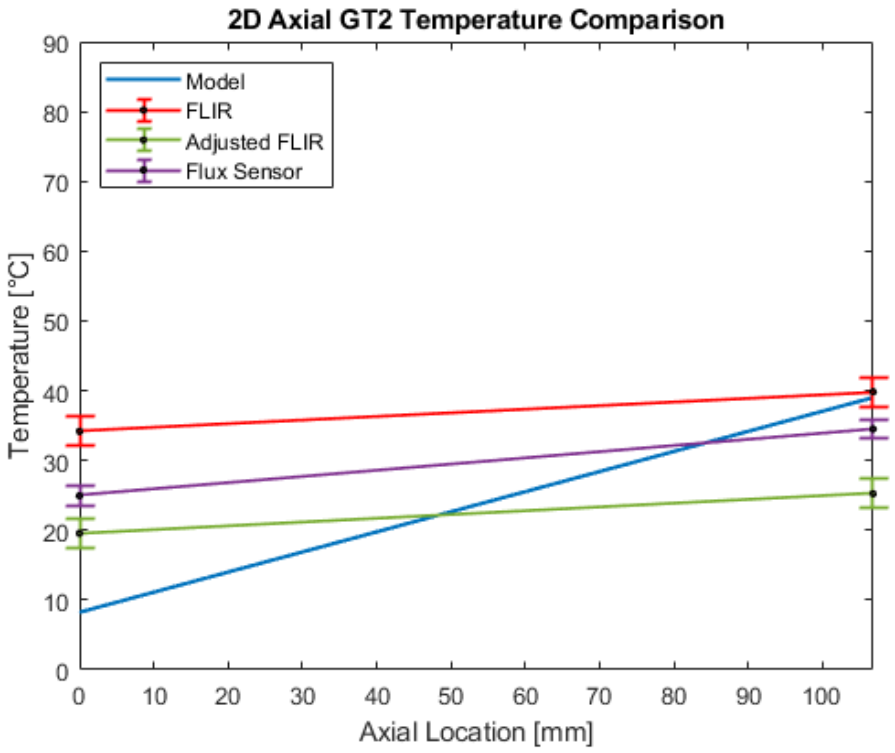

(36f)

Figure 36 – Updated temperature comparison between 1D and 2D steady-state measured and design tool results. 36a: 1D KT1, 36b: 1D KT2, 36c: 1D GT1, 36d: 1D GT2, 36e: 2D GT1, 36f: 2D GT2

Shifted temperature models correlate well with measured data, with an average temperature difference on the order of 10e-7°C, less than 1%. This shift provides useful information when calculating practical responses, accounting for losses and design tool assumptions rather than theoretical values. Similar to thermal conductivity comparisons, the design tool retains the ability to calculate theoretical temperatures while also providing this temperature shift capability.

CHAPTER 5. CONCLUSIONS

The design tool provides both theoretical results and results adjusted for practical losses. Theoretical results overestimate thermal conductivity and underestimate temperature. Comparing design tool results to measured data provides realistic adjustment factors for both thermal conductivity and temperature calculations. These factors provide the ability to estimate important parameters, taking losses and design tool assumptions into account. With these adjustment factors the modeled conductivities differ from measured values by 3.7% on average, and modeled overall temperatures differ from measured temperatures by less than 1%. These factors allow the user to fine-tune the design tool as more measured results become available. Both 1D and 2D modeled temperature contours correlate visually with measured contours. Variable inputs such as geometry, mesh type, stacked mesh, materials, and pillar type provide a flexible design tool allowing engineers to model theoretical parameters alongside practical results.

Future work for this effort may include user interface updates and performing a parameterization study using the design tool. The current design tool provides an input section for the user with all possible inputs, and makes use of multiple comments to guide the user experience. Matlab does provide graphical user interface tools which, if implemented correctly, may provide a more straightforward user interface. A parameterization study examining the implications of changing various internal parameters would provide interesting information to design engineers as well. For instance, what impact would a single mesh have on capillary transport compared to the hybrid wicking structure used in this effort? It may also be useful to examine the magnitude of heat losses

to the environment from the top surface of the TGP during testing. This would give insight into how measured temperatures and conductivities in this testing may compare to measured temperatures and conductivities using vacuum insulation. Although this may be an interesting project, it would provide information about measured results and adjustment factors rather than design tool results. As the purpose of this effort is to create a design tool to benefit the design engineer, future work which provides the best design tool experience may be more beneficial. This work may include the parametrization study and user interface updates.

REFERENCES

[1] Liu, T., Dunham, M.T., Jung, K., Chen, B., Asheghi, M., Goodson, K. 2020. "Characterization and Thermal Modeling of a Miniature Silicon Vapor Chamber for Die-Level Heat Redistribution". International Journal of Heat and Mass Transfer, Vol. 152. pp. 119569.

[2] Lewis, R., Xu, S., Liew, L., Coolidge, C., Yang, R. Lee, Y. 2015. "Thin Flexible Thermal Ground Planes: Fabrication and Scaling Characterization." Journal of Microelectromechanical Systems, Vol. 24, No. 6, pp. 2040-2048.

[3] Ranjan, R., Murthy, J.Y., Garimella, S.V., Vadakkan, U. 2011. "A Numerical Model For Transport in Flat Heat Pipes Considering Wick Microstructure Effects." International Journal of Heat Mass Transfer, Vol. 54, pp. 153–168.

[4] Patankar, G., Weibel, J.A., Garimella, S.V. 2020. "On the Transient Thermal Response of Thin Vapor Chamber Heat Spreaders: Optimized Design and Fluid Selection." International Journal of Heat and Mass Transfer, Vol. 148. pp. 119106.

[5] Ravi S., Dharmarajan, R., Moghaddam, S. 2016. "Physics of Fluid Transport in Hybrid Biporous Capillary Wicking Microstructures." Langmuir, Vol. 32 (33), pp. 8289-8297.

[6] Yang, R., Lee, Y., Bright, V.M., Li, C., Oshman, C., Shi, B., Cheng, J., Peterson, G.P. 2020. “Thermal Ground Plane”. (US Patent No. 10,571,200 B2). U.S. Patent and Trademark Office.

[7] Peterson, G.P. 1994. “An Introduction to Heat Pipes: Modeling, Testing, and Applications.” New York (NY): John Wiley & Sons.

[8] Lee, H. 2017. “Thermoelectrics: Design and Materials.” New York (NY): John Wiley & Sons.

[9] McNally, D.P., Lewis, R., Lee, Y.C. 2019. “Characterization of Hybrid Wicking Structures for Flexible Vapor Chambers.” Journal of Electronic Packaging, Vol. 141, No. 1.

[10] Young, H.D. 1962. “Statistical Treatment of Experimental Data.” New York (NY): McGraw-Hill.